A&A 465, 129–145 (2007)
DOI: 10.1051/0004-6361:20053555

Astronomy & Astrophysics

Modeling optical and UV polarization of AGNs

I. Imprints of individual scattering regions

R. W. Goosmann[1,2] and C. M. Gaskell[3]

[1] Astronomical Institute of the Academy of Sciences, Bočni II 1401, 14131 Prague, Czech Republic
e-mail: goosmann@astro.cas.cz
[2] Observatoire de Paris – Meudon, 5 place Jules Janssen, 92190 Meudon, France
[3] Department of Physics & Astronomy, University of Nebraska, Lincoln, NE 68588-0111, USA
e-mail: mgaskell1@unl.edu

Received 2 June 2005 / Accepted 22 December 2006

ABSTRACT

Context. Spectropolarimetry of AGNs is a powerful tool for studying the structure and kinematics of the inner regions of quasars.
Aims. We wish to investigate the effects of various AGN scattering region geometries on the polarized flux.
Methods. We introduce a new, publicly available Monte Carlo radiative transfer code, STOKES, which models polarization induced by scattering off free electrons and dust grains. We model a variety of regions in AGNs.
Results. We find that the shape of the funnel of the dusty torus has a significant impact on the polarization efficiency. A compact torus with a steep inner surface scatters more light toward type-2 viewing angles than a large torus of the same half-opening angle, θ_0. For $\theta_0 < 53°$, the scattered light is polarized perpendicularly to the symmetry axis, whilst for $\theta_0 > 60°$ it is polarized parallel to the symmetry axis. In between these intervals the orientation of the polarization depends on the viewing angle. The degree of polarization ranges between 0% and 20% and is wavelength independent for a large range of θ_0. Observed wavelength-independent optical and near-UV polarization thus does not necessarily imply electron scattering. Spectropolarimetry at rest-frame wavelengths less than 2500 Å may distinguish between dust and electron scattering but is not conclusive in all cases. For polar dust, scattering spectra are reddened for type-1 viewing angles, and made bluer for type-2 viewing angles. Polar electron-scattering cones are very efficient polarizers at type-2 viewing angles, whilst the polarized flux of the torus is weak.
Conclusions. We predict that the net polarization of Seyfert-2 galaxies decreases with luminosity, and conclude that the degree of polarization should be correlated with the relative strength of the thermal IR flux. We find that a flattened, equatorial, electron-scattering disk, of relatively low optical depth, reproduces type-1 polarization. This is insensitive to the exact geometry, but the observed polarization requires a limited range of optical depth.

Key words. galaxies: active – polarization – radiative transfer – scattering

1. Introduction

One of the foremost problems in AGN research is that the innermost regions of AGNs cannot be resolved in the optical and UV with current technology. However, the light of AGNs is polarized over a broad wavelength range, and this allows us to put important constraints on the geometry of the emitting and scattering regions. Spectropolarimetric observations giving the detailed wavelength dependence of the polarized flux give further clues to the nature of the polarizing mechanism.

Our inferences of the innermost structures of AGNs have so far been obtained indirectly. Rowan-Robinson (1977) suggested that AGNs are surrounded by a dusty torus and in the same paper he gives a suggestion by Penston that Seyfert 2 galaxies are seen close to edge-on so that the active nucleus is obscured by the torus. Support for this picture came from the important discovery by Keel (1980) that Seyfert 1 galaxies (active galaxies showing a broad-line region; BLR) are preferentially seen face-on. Keel (1980) also investigated absorption effects inside the host galaxies and emphasized the need of additional nuclear absorption in Seyfert galaxies with respect to normal spirals. Keel's work led to further confirmation of the importance of orientation effects (Lawrence & Elvis 1982; De Zotti & Gaskell 1985). Since then, the dusty-torus model has become the standard unified model (see Antonucci 1993) dividing AGNs into two sub-types: "type-1" AGNs which are seen close to face-on, and "type-2" AGNs which are seen close to edge-on. In type-1 AGNs the central energy source and its surroundings (e.g., the BLR) can be seen, whilst in type-2 AGNs the torus blocks our direct view of these inner regions. While this obscuration and the IR emission from the torus are the most obvious effects of the torus, scattering from the dust will add polarized flux. The polarization spectrum of an optically thick dusty torus has been the subject of several modeling projects (Kartje 1995; Wolf & Henning 1999; Watanabe et al. 2003).

When Dibai & Shakhovskoy (1966) and Walker (1966) discovered optical polarization of AGNs, it was initially taken to be evidence of optical synchrotron emission, since synchrotron radiation has a high intrinsic polarization. However, Angel et al. (1976) found the Balmer lines in NGC 1068 to be polarized similarly to the continuum, thus implying that scattering was responsible for the polarization of both the lines and continuum. The difference they found in polarization between the narrow-line region (NLR) and BLR places the scattering region outside the BLR, but inside the NLR.

When light is scattered, the angle of polarization depends on the direction of the last scattering, so one expects the angle of polarization to be related to the structure of the AGN. Stockman et al. (1979) made the seminal discovery that for low-polarization, high optical luminosity, radio-loud AGNs, the optical polarization position angles tend to align *parallel* to the large-scale radio structure. Although they interpreted this as a consequence of optical synchrotron emission, they also suggested that polarization from an optically-thin, non-spherically-symmetric scattering region near the source of optical radiation was another possibility.

Antonucci (1982) pointed out that whilst many radio galaxies showed a similar parallel alignment of the polarization and radio axes, there was, unexpectedly, a population showing a *perpendicular* relationship. It was subsequently shown (Antonucci 1983) that relatively-radio-quiet Seyfert galaxies show a similar dichotomy between the predominantly, but not exclusively, parallel polarization in face-on type-1 Seyferts and the perpendicular polarization of type-2 Seyferts (see Antonucci 1993, 2002, for reviews). These discoveries made a synchrotron origin of the polarization much less likely.

Polarization perpendicular to the axis of symmetry is easily produced by scattering off material close to the axis. There is good observational evidence for the existence of ionization cones along the polar axis in numerous objects (see Kinney et al. 1991, and reference therein). Polar scattering has been particularly well studied in the Seyfert-1 galaxy NGC 1068. Antonucci & Miller (1985) made the key discovery that the polarized-flux spectrum can offer a periscope view of type-2 AGNs because much of the polarized flux originates inside the torus. Detailed HST polarimetry has revealed the polarization structure of the ionization cones (see Capetti et al. 1995a,b; Kishimoto 1999).

The detection of a hidden broad-line region in NGC 1068 by Antonucci & Miller (1985) was of great importance for AGN research since it provided strong support for the unified theories of AGN activity. More hidden type-1 nuclei have subsequently been found by analysis of their polarized-flux spectra (see e.g., Miller & Goodrich 1990; Tran et al. 1992; Hines & Wills 1993; Kay 1994; Heisler et al. 1997; Tran 2001; Smith et al. 2004). Similar work on the radio galaxy 3C 321 was done by Young et al. (1996), and Tran et al. (1999) could identify an active nucleus inside an ultra-luminous infra-red galaxy using spectropolarimetry. Recently, hidden type-1 nuclei have also been found in five type-2 quasar candidates (Zakamska et al. 2005).

The new generation of large telescopes is delivering spectropolarimetry of emission line profiles with good velocity resolution (see, for example, the spectropolarimetry of the Seyfert 1.5 galaxy NGC 4151 presented by Martel 1998, and the atlas of spectropolarimetry of Seyfert galaxies presented by Smith et al. 2002). Examination of velocity-dependent polarization of emission lines promises to reveal valuable information about the geometry of the BLR (Smith et al. 2005). Similarly, spectropolarimetry of quasar absorption lines helps to constrain the geometry of broad absorption line QSOs (Goodrich & Miller 1995; Cohen et al. 1995; Hines & Wills 1995; Ogle et al. 1999).

In order to understand these many facets of AGN polarization, and their implications for the underlying geometry, theoretical modeling is necessary. Analytical approaches to radiative transfer that have been carried out so far are generally limited to the consideration of single-scattering models. Computer simulations are needed to investigate multiple-scatterings. In this paper we describe STOKES, a new general-purpose, publicly-available[1], Monte Carlo code for modeling wavelength-dependent polarization in a wide variety of scenarios, and we present some results of our study of AGN polarization.

In this paper we confine ourselves to using STOKES for calculating the polarization imprints of basic constituents of the unified scheme. We compute the polarization spectrum of dusty tori with various geometries and opening angles, and we consider scattering in polar cones and electron disks. We investigate the effects of geometrical shape and optical depth of given regions. None of our models are intended to reproduce observational polarimetric data for any specific object. Rather, we want to investigate general constraints on the scattering regions and the geometry of AGNs. We discuss consequences for the observed polarization dichotomy between type-1 and type-2 objects. We leave aside the question of interactions between different types of scattering regions for paper II (Goosmann & Gaskell, in preparation) where we also conduct more detailed modeling of AGNs in the unified scheme.

The present paper is organized as follows: in Sect. 2 we summarize modeling of optical and UV polarization of AGN and the main results obtained previously. Section 3 describes our code STOKES. In Sect. 4 we present modeling results for equatorial, toroidal dust distributions. Section 5 is dedicated to electron and dust scattering in polar double-cones. In Sect. 6 we investigate the polarization signature of equatorial regions for electron scattering. Our results are discussed in Sect. 7 and we give some conclusions in Sect. 8.

2. Previous codes and modeling

In this section, we briefly summarize some recent AGN polarization modeling codes which we will compare our STOKES modeling with.

Young et al. (1995, 1996), Packham (1997), and Young (2000) developed an analytical radiative transfer model, the Generic Scattering Model (GSM), for polarization modeling. The model is based on the unified AGN model. Extended emission regions can be defined, and scattering processes as well as dichroic absorption are considered. The modeled geometries include toroidal, disk-like, and conical regions of dust and free electrons. For scattering material in motion, Doppler effects are included. The model is fairly effective in reproducing spectropolarimetric data of Seyfert galaxies (see, for example, Young et al. 1999, for Mrk 509). In particular, it reproduces variations of the polarization across broad emission lines (Smith et al. 2005). The model is semi-analytical and therefore does not take multiple scattering into account.

Wolf & Henning (1999) present a Monte-Carlo code used to compute the polarization obtained by scattering inside axisymmetric regions. They consider dust and electron scattering for polar double-cones and equatorial tori. In the Monte-Carlo approach two or more of such components can be combined and the resulting polarization spectra are modeled for various inclinations of the system. Aside from spectropolarimetric modeling, the code by Wolf & Henning (1999) can also produce polarization images, which are provided for various torus geometries. An important element in this code is that multiple scattering, which becomes important for optical depths >0.1, is considered accurately by including the dependence of the scattering angle and the polarization of a scattered photon on its incident Stokes vector. For dust scattering, two different grain size

[1] http://www.stokes-program.info/

distributions were examined: one parameterization representing Galactic dust, and the other favoring larger grains.

Kartje (1995) also developed a Monte Carlo Code and investigated quasar schemes with either a torus geometry or conical stratified winds along the polar axis. In addition to polarization by scattering, he also considers polarization by dichroic extinction due to magnetically-aligned dust grains. For a simple unified torus model he finds that the dominant parameter of the polarization, P, is the torus half-opening angle: for type-2 objects one can find significant polarization (up to 30%) with a position angle directed perpendicular to the axis of symmetry; for type-1 objects P is negligible. Kartje obtains an important result when he investigates conical stratified-wind regions containing free electrons closer to the central source and dust farther out: the amount of polarization ranges between 0% and 13%, matching observed values, and the direction of the $\boldsymbol{E}$-vector depends on the viewing angle in a manner that agrees with the above-mentioned type-1/type-2 dichotomy. The polarization percentage can be increased if there is magnetic alignment of dust grains, but the general dependence of P on the viewing angle seems to be a geometrical effect.

Another Monte-Carlo polarization code is presented by Watanabe et al. (2003). It is applied to modeling of optical and near-infrared spectropolarimetric data of the type-2 Seyfert galaxies Mrk 463E, Mrk 1210, NGC 1068, and NGC 4388. The code contains electron and dust scattering routines quite similar to those used by Wolf & Henning (1999). It considers multiple scattering and dichroic absorption in dusty tori, spheres as well as electron and dust scattering in double-conical regions. The absorption and scattering properties of the dust are carefully calculated by Mie theory. Watanabe et al. (2003) examine wavelength-dependent polarization properties for different geometries over a broad-wavelength range and give constrains about possible scattering components within the objects they observed. They conclude that a combination of dust and electron scattering in polar regions can reproduce the optical polarization properties of Mrk 463E and Mrk 1210. The slope of optical polarization in NGC 1068 is almost flat favoring electron scattering as the dominant polarizing process. For the near-infrared range polarization of these objects can be modeled by dichroic absorption of aligned dust grains in a torus. However, scattering off Galactic dust in a torus cannot simultaneously reproduce the near-infrared polarization and the total flux. Watanabe et al. (2003) hence suggest that the grain size composition of AGNs might be different from our Galaxy.

This list of previous polarization modeling is not exhaustive. For example, Blaes & Agol (1996) and Agol & Blaes (1996) have presented modeling of the wavelength-dependent polarization signature of accretion disks at the Lyman limit, and Kishimoto (1996) modeled polarization due to electron-scattering off clumpy media in polar regions of AGN. Also, a new Monte-Carlo model, which includes polarization transfer for the continuum and for broad quasar absorption lines, was recently presented by Wang et al. (2006). We have restricted this brief review to recent modeling of polarization by dust and electron scattering, since this is our primary concern in the present paper.

3. Stokes – an overview

The computer program STOKES performs simulations of radiative transfer, including the treatment of polarization, for AGNs and related objects. The code is based on the Monte Carlo method and follows single photons from their creation inside the source region through various scattering processes until they become absorbed or manage to escape from the model region (Fig. 1). The polarization properties of the model photons are given by their stored Stokes vectors.

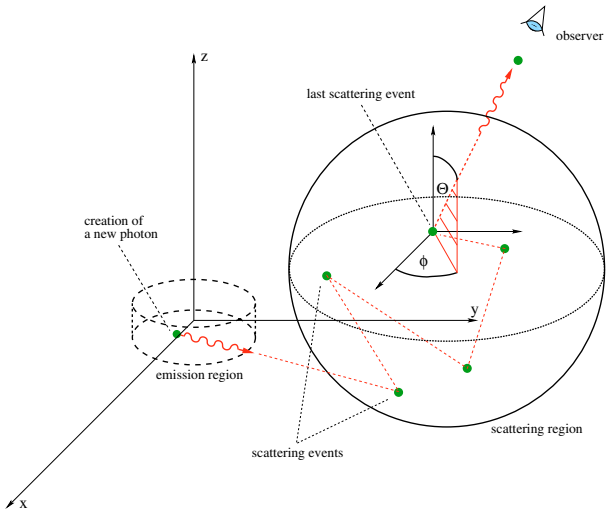

Fig. 1. A photon working its way through the model space.

Photons are created inside the source regions, which can be realized by different geometries. The continuum radiation is normally simply defined by the index α of an $F_\nu \propto \nu^{-\alpha}$ power law. The Stokes vectors of the photons are initially set to the values of completely unpolarized light.

Various scattering regions can be arranged around the sources. The program offers e.g. toroidal, cylindrical, spherical or conical shapes. These regions can be filled with free electrons or dust consisting of "astronomical silicate" and graphite. A photon works its way through the model region and generally undergoes several scatterings. The emission directions, path lengths between scattering events, and the scattering angles are computed by Monte Carlo routines based on classical intensity distributions. During each scattering event the Stokes vector is changed by multiplication with the corresponding Mueller matrix. For dust scattering, absorption is important, and a large fraction of the photons never reaches the virtual observer. The relevant cross sections and matrix elements for dust scattering and absorption are computed on the basis of Mie theory applied to size distributions of spherical graphite and silicate grains.

If a photon escapes from the model region, it is registered by a web of virtual detectors arranged in a spherical geometry around the source. The flux and polarization information of each detector is obtained by adding up the Stokes parameters of all detected photons. If the model is completely axially symmetric these can be azimuthally integrated and, if there is plane symmetry, the top and bottom halves are combined. The object can be analyzed in total flux, in polarized flux, percentage of polarization, and the position angle at each viewing angle. The light travel time of each photon is also recorded, so it is possible to model time-dependent polarization (Gaskell et al., in preparation).

3.1. Monte Carlo method, photon initialization, and sampling the free path length

Using the Monte Carlo method it is possible to generate a random event x according to a given probability density distribution $p(x)$. Let $p(x)$ be defined on the interval $[0, x_{\max}]$. We can

then construct the probability distribution function $P(x)$ and relate it to a random number, r, between 0 and 1 as follows:

$$r = P(x) = \frac{1}{C}\int_0^x p(x')\mathrm{d}x'. \quad (1)$$

The constant C is a normalization constant resulting from integration over the whole definition interval $[0, x_{\max}]$. Given the random number, the corresponding value of x for a single event is obtained by inverting Eq. (1). A good description of the Monte Carlo method can be found in Cashwell & Everett (1959). In the following, we describe the main routines of STOKES and denote all random numbers computed from equation (1) by r_i, with $i = 1, 2, 3....$

To generate a model photon, its initial parameters of position, direction of flight, and wavelength all have to be set. Different geometries for the continuum region, broad-line region, and narrow-line region are available in STOKES. Assuming a constant density of the emitting material, a random position for the new photon is sampled. The flight direction is given by two angles, θ and ϕ, defined with respect to a standard polar coordinate system. Assuming isotropic emission, the sampling equations for the angles are as follows:

$$\theta = \arccos(1 - 2r_1), \quad (2)$$

$$\phi = 2\pi r_2. \quad (3)$$

The wavelength of the photon is sampled according to the intensity spectrum over a range $[\lambda_{\min}, \lambda_{\max}]$. This leads to:

$$\lambda = \begin{cases} \left[\lambda_{\min}^{\alpha} + r_3\left(\lambda_{\max}^{\alpha} - \lambda_{\min}^{\alpha}\right)\right]^{\frac{1}{\alpha}}, & \text{for } \alpha \neq 1, \\ \lambda_{\min}\left(\frac{\lambda_{\max}}{\lambda_{\min}}\right)^{r_3}, & \text{for } \alpha = 1. \end{cases} \quad (4)$$

Here, α denotes the usual power law index of the intensity spectrum.

If we ignore scatterings back into the beam, the intensity of a photon beam traversing a slab of scattering material with particle number density N and cross-section σ will drop by a factor of $e^{N\sigma l}$, with l being the distance traveled inside the scattering region. From this, one can derive the sampling function of l:

$$l = \frac{1}{N\sigma}\ln(1 - r_4). \quad (5)$$

The factor $\frac{1}{N\sigma}$ is the mean free path length. Depending on the scattering material, the program uses either a dust extinction cross-section σ_{ext} computed from Mie theory or, in case of electron scattering, the Thomson cross section σ_{ES}.

3.2. Polarization formalism, scattering, and photon detection

The polarization properties of the photons sampled in STOKES and their transformation during scattering events rely on previous work described e.g. in Fischer et al. (1994). The theoretical basis for the formalism presented in this section can be found in Bohren & Huffman (1983).

If we consider a photon being scattered off a spherical particle (see Fig. 2), the outgoing electromagnetic wave associated with the photon can be resolved into two components, $E_{\parallel}$ and $E_{\perp}$. These components refer to directions of the electric-field vector parallel and perpendicular to the scattering plane. For scattering off a spherical particle, the following relation between the incoming and scattered electric fields holds:

$$\begin{pmatrix} E_{\parallel,\mathrm{s}} \\ E_{\perp,\mathrm{s}} \end{pmatrix} = \begin{pmatrix} S_2(\theta) & 0 \\ 0 & S_1(\theta) \end{pmatrix}\begin{pmatrix} E_{\parallel,\mathrm{i}} \\ E_{\perp,\mathrm{i}} \end{pmatrix}. \quad (6)$$

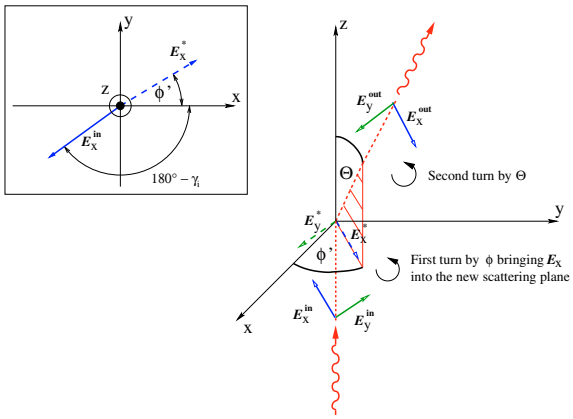

Fig. 2. Geometry and denotations for a single scattering event. The inset shows the first rotation of the $\boldsymbol{E}$-vector by the angle ϕ, the view on the polarization plane is along the negative z-axis.

The scattering matrix elements, $S_1(\theta)$ and $S_2(\theta)$, are independent of the azimuthal angle ϕ. In case of Thomson scattering, there absolute values obey to simple analytic expressions:

$$|S_1(\theta)|^2 = 1, \quad (7)$$

$$|S_2(\theta)|^2 = \cos^2\theta. \quad (8)$$

For dust scattering, the albedo and the matrix elements of a standard dust grain are calculated from Mie theory (see Sect. 3.3). The albedo at the photon wavelength is compared to a random number, r_5, in order to decide whether the photon is absorbed or scattered. If the photon is absorbed it is lost, and the cycle starts over with the generation of a new photon.

The polarization vector of each photon lies perpendicular to its trajectory, inside the so-called polarization plane, and denotes the preferred direction of the $\boldsymbol{E}$-vector. It is defined with respect to a co-moving coordinate system. The polarization information of each photon is coded by four Stokes parameters I, Q, U, and V, representing the 4-dimensional Stokes vector. We assume that newly created photons coming from the source are unpolarized. Hence, their Stokes vectors have the simple form:

$$\begin{pmatrix} I \\ Q \\ U \\ V \end{pmatrix} = \begin{pmatrix} 1 \\ 0 \\ 0 \\ 0 \end{pmatrix}. \quad (9)$$

With each scattering event, the co-moving coordinate system undergoes a double rotation: the first rotation, by the azimuthal angle ϕ, occurs around the current flight direction of the photon. It rotates the $\boldsymbol{E}$-vector inside the polarization plane to the position of the new scattering plane (see Fig. 2). Physically, it does not affect the polarization state, although the Stokes vector undergoes the following coordinate transformation.

$$\begin{pmatrix} I^* \\ Q^* \\ U^* \\ V^* \end{pmatrix} = \begin{pmatrix} 1 & 0 & 0 & 0 \\ 0 & \cos 2\phi & \sin 2\phi & 0 \\ 0 & -\sin 2\phi & \cos 2\phi & 0 \\ 0 & 0 & 0 & 1 \end{pmatrix}\begin{pmatrix} I^{\mathrm{in}} \\ Q^{\mathrm{in}} \\ U^{\mathrm{in}} \\ V^{\mathrm{in}} \end{pmatrix}. \quad (10)$$

The second rotation occurs in the scattering plane by the scattering angle θ. The change of the Stokes vector is determined by the Mueller matrix, which for scattering off a spherical particle has the form:

$$\begin{pmatrix} I^{\mathrm{out}} \\ Q^{\mathrm{out}} \\ U^{\mathrm{out}} \\ V^{\mathrm{out}} \end{pmatrix} = \begin{pmatrix} S_{11} & S_{12} & 0 & 0 \\ S_{12} & S_{22} & 0 & 0 \\ 0 & 0 & S_{33} & S_{34} \\ 0 & 0 & -S_{34} & S_{44} \end{pmatrix}\begin{pmatrix} I^* \\ Q^* \\ U^* \\ V^* \end{pmatrix}. \quad (11)$$

The entries of the Mueller matrix are obtained by simple relations from the elements of the scattering matrix, $S_1(\theta)$ and $S_2(\theta)$.

The angle-dependent classical intensity distribution of a scattered electromagnetic wave measures the probability of finding a scattered photon at a given direction. Such probability density distributions are derived from Eq. (6). An important aspect included in STOKES is that the scattering direction is sampled depending on the incident polarization vector. The degree P_i and the position angle γ_i of the polarization before scattering are computed from the incident Stokes vector and enter the sampling equations of θ and $\phi = \phi' + 180° - \gamma_\mathrm{i}$:

$$P(\theta) = N \int_0^\theta \left(|S_1(\theta')|^2 + |S_2(\theta')|^2\right) \sin(\theta') \mathrm{d}\theta', \tag{12}$$

$$P_\theta(\phi') = \frac{1}{2\pi}\left(\phi' - \frac{|S_1(\theta)|^2 - |S_2(\theta)|^2}{|S_1(\theta)|^2 + |S_2(\theta)|^2} P_\mathrm{i} \frac{\sin 2\phi'}{2}\right). \tag{13}$$

The number N is a normalization constant in order to have (12) range from 0 to 1 for scattering angles between 0° and 180°. To sample ϕ and θ, the right hand-sides of these equations have to be set equal to random numbers r_6, r_7. The equations are then solved for the angles.

Note that the sampling is independent of the incident polarization for θ but not for ϕ. In several Monte-Carlo polarization transfer codes described in the literature, the incident polarization does not affect the sampling of the scattering angles. This does not present a problem if one considers unpolarized incident radiation and low optical depths. Also for very high optical depths, when multiple-scattering neutralizes the polarization inside the scattering region, the incident polarization can be neglected. However, results for intermediate optical depths are sensitive to the sampling method and they should consider the polarization state of the incident photon.

When a photon escapes from the model region it is recorded by one of the virtual detectors. It is then necessary to rotate the polarization plane around the flight direction until it matches the reference axis of the detector. The Stokes vectors of all incoming photons can finally be added up to the values $\hat{I}$, $\hat{Q}$, $\hat{U}$ and $\hat{V}$. The net polarization properties are derived from:

$$P = \frac{\sqrt{\hat{Q}^2 + \hat{U}^2 + \hat{V}^2}}{\hat{I}}, \tag{14}$$

$$\gamma = \frac{1}{2} \arctan \frac{\hat{U}}{\hat{Q}}. \tag{15}$$

3.3. Computation of dust properties

Mathis et al. (1977, MRN) suggested dust compositions to reproduce extinction curves observed in our Galaxy. They assumed various types of dust grains having a size distribution proportional to a^s, with a being the grain radius and s an arbitrary power-law index. Our parameterization of the dust properties follows that of MRN and gives a good description of observed Galactic extinction curves. The user can choose the arbitrary minimum and maximum radii of the grain-size distribution, its power law index, and the relative abundances of graphite and "astronomical silicate".

The results from Mie scattering theory, i.e., scattering and extinction cross sections, albedos, and elements of the scattering matrix, are computed using the code given by Bohren & Huffman (1983). We imported complex dielectric functions for graphite and silicate measured by Draine & Lee (1984). For graphite, two dielectric functions have to be considered since the optical properties for light polarized parallel and perpendicular to the crystals axis differ from each other. The code therefore works with the two different graphite types having abundances in a ratio of 1:2. It computes a weighted average for the dust composition and grain size distribution defined. The procedure is described, for example, in Wolf (2003). The properties of the resulting "standard dust grain" are then used by all dust-related routines of STOKES.

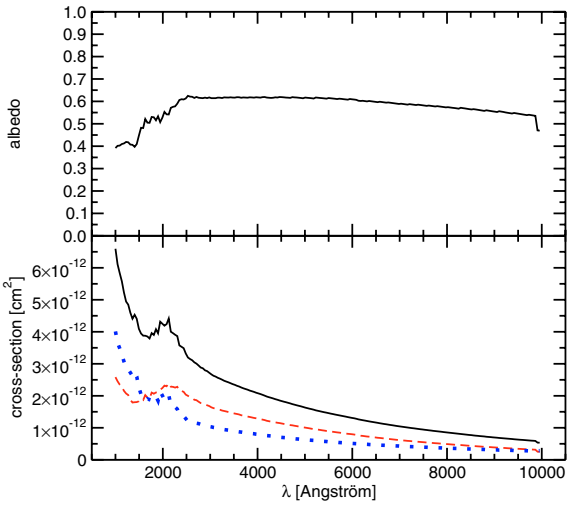

Fig. 3. Characteristic properties of the dust composition adopted for this paper as a function of wavelength. *Top*: albedo value. *Bottom*: cross-sections for extinction (black, solid), scattering (red, dashed), and absorption (blue, dotted).

We confine ourselves to using standard Galactic dust such as is seen in the solar neighborhood, even though there is evidence that the tori of AGNs might have different compositions and grain size distributions (see Czerny et al. 2004; Gaskell et al. 2004; and Gaskell & Benker 2006). Following Wolf & Henning (1999), we parameterize Galactic dust by a mixture of 62.5% carbonaceous dust grains and 37.5% "astronomical silicate". We consider grain radii, a, from 0.005 μm to 0.250 μm with a distribution $n(a) \propto a^s$ with $s = -3.5$. The resulting cross-sections and the albedo are shown in Fig. 3 as a function of wavelength. The figure shows that for this particular dust model, the albedo is rather flat with a value of 0.55−0.6 over the wavelength range considered. For wavelengths $\lesssim$2500 Å it falls to 0.4. The cross-sections all decrease regularly with wavelength, with the exception of the well-known hump around 2175 Å.

4. Simulation of torus geometries

In this section we investigate how much of the polarization properties of type-1 and type-2 AGNs can be produced by a uniform-density torus alone. Kartje (1995) modeled the polarization induced by scattering off a cylindrically shaped torus. Their torus model was adopted from a fit to NGC 1068 given by Pier & Krolik (1992). This torus is geometrically rather compact and is located within a radius of 1 pc from the central source. Such a cylindrical torus is not necessarily physical, so we examine whether the results of Kartje can be confirmed with more general tori, and we extend the range of parameter space explored.

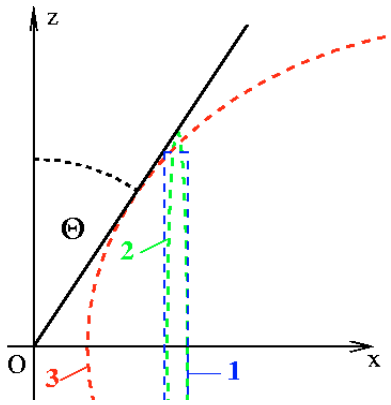

Fig. 4. Geometry of the three torus models we consider: (1) the cylindrical torus used by Kartje, (2) a compact elliptically-shaped torus, and (3) an extended elliptical torus. All tori have the same half-opening angle Θ_0

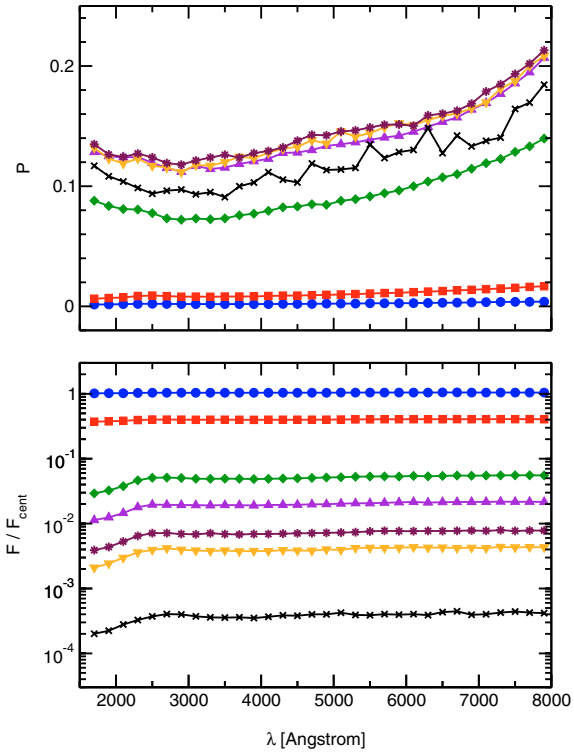

Fig. 5. Modeling a cylindrical torus with an elliptical cross-section and $\theta_0 = 30°$ (see Sect. 4.1). *Top*: polarization, *P*. *Bottom*: the fraction, F/F_*, of the central flux, F_*, seen at different viewing inclinations, i. Legend: $i = 87°$ (edge-on) (black crosses), $i = 76°$ (orange triangles with points down), $i = 70°$ (intermediate) (maroon stars), $i = 57°$ (purple triangles with points up), $i = 41°$ (green diamonds), $i = 32°$ (red squares), and $i = 18°$ (face-on) (blue circles).

4.1. Curved surfaces versus sharp edges

The dusty tori examined by Kartje (1995), Wolf & Henning (1999), Young (2000), and Watanabe et al. (2003) have rather sharp edges, and, since we find that polarization results can depend strongly on geometrical details, we have investigated a less artificial torus geometry with an elliptical cross-section. To examine the influence of sharp edges of the cylindrical torus on the polarization, we define a torus with similar dimensions, and the same optical depth in the V band (τ_V) $\sim$ 750 along the radius in the equatorial plane. Thus, practically no photon is able to penetrate through the torus and only scattering off its surface is relevant. However, our torus has an elliptical cross-section (see Fig. 4) instead of the rectangular cross-section used by Kartje.

Our results compare very well to those obtained by Kartje (1995). In Fig. 5 we show polarization and flux (normalized to the flux of the central source) versus wavelength at different viewing directions. The torus considered has a half-opening angle of $\theta_0 = 30°$. The positive values of P denote that the polarization vector is oriented perpendicularly to the symmetry axis (type-2 polarization). In our simulations the torus is filled with standard Galactic dust, parameterized as described at the end of Sect. 3. We sample a total of 10^8 photons and record spectra at 10 different viewing angles scaled in $\cos i$, where i is measured from the axis of the torus. We show our results as a function of $\cos i$ because it gives equal flux per bin for an isotropic source located at the center of the model space if there is no scattering. Our figure is quite similar to the corresponding diagrams in Kartje's paper (see his Fig. 5).

The only difference between our results and those of Kartje is that we generally obtain slightly lower polarization degrees and a slightly different wavelength-dependent slope for the scattered flux. This can be explained by the fact that we calculate our cross-sections from Mie theory of a specific dust composition whilst Kartje used cross-sections given by Mezger et al. (1982).

We also investigated the polarization of a compact torus with an elliptical cross-section for changing θ_0. Again we obtained similar results (not shown) to those for Kartje's cylindrically-shaped tori. Thus, the differences in polarization between the elliptical and cylindrical tori are negligible. Having sharp edges in the cylindrical model rather than the more realistic rounded edges of the elliptical torus does not introduce spurious effects.

4.2. The effect of the shape of the inner edge of the torus

A real torus is undoubtedly thicker than the geometrically thin cylindrical torus of Kartje. Direct imaging of NGC 4261 (=3C 270) shows that the dusty torus in that AGN extends out to 230 pc (Ferrarese et al. 1996). A similar dust lane across the nucleus of M 51 (=NGC 5194) extends by ~100 pc (Ford et al. 1992). The inner radii of tori are obtained by infra-red reverberation mapping of the hot dust and are in the range of tens to hundreds of light-days for Seyfert galaxies (see Glass 2004; and Suganuma et al. 2006).

The outer regions of tori have considerable optical depth, so their precise shape is unimportant, since no photons escape parallel to the equatorial plane of the torus. The shape of the inner region facing the central energy source is more relevant. Current torus models commonly consider inner surfaces that are convex towards the central source. We thus model optically-thick, uniform-density tori with elliptical cross sections, an inner radius of 0.25 pc, and an outer radius of 100 pc. We compare these results to the modeling of a more compact torus with the same half-opening angle, $\theta_0 = 30°$, as in Sect 4.1. We determine the dust density by fixing τ_V at ~750. Variability observations imply that the size of the optical and UV-continuum source in Seyfert galaxies is less than a few light-days, as is also expected from simple black-body emissivity arguments. Hence, when considering scattering off the torus, we can neglect the finite size of the continuum source in our model and assume a point-like emission region. Note that this consideration remains valid for objects with higher luminosities because both the size of the

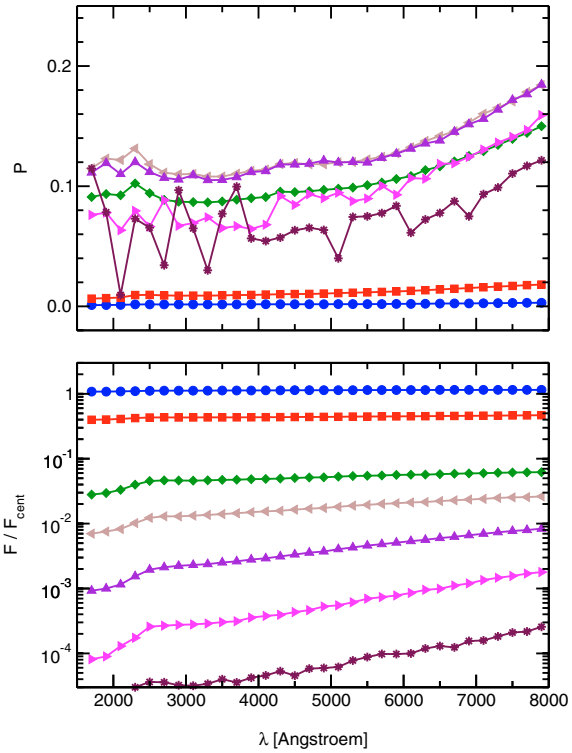

Fig. 6. Modeling a large torus with an elliptical cross-section and $\theta_0 = 30°$ (see Sect. 4.2). *Top*: polarization, P. *Bottom*: the fraction, F/F_*, of the central flux, F_*, seen at different viewing inclinations, i. Legend: $i = 70°$ (intermediate) (maroon stars), $i = 63°$ (pink triangles with points to the right), $i = 57°$ (purple triangles with points up), $i = 49°$ (brown triangles with points to the left), $i = 41°$ (green diamonds), $i = 32°$ (red squares), and $i = 18°$ (face-on) (blue circles)

central emission region and the inner radius of the torus scale with luminosity.

The resulting spectra at different inclinations are shown in Fig. 6. If the viewing angle, i, is less than θ_0 (thus corresponding to a type-1 object), we only observe a regular type-1 spectrum. We find that there is no significant polarization in this case. If we look at a type-2 object at a higher inclination angle, only scattered (and hence polarized) light is detected. This is analogous to the results obtained for the compact torus shown in Fig. 5. The overall shape of the polarization spectrum for both sizes of the torus is rather similar as well. With increasing viewing angle the level of the polarization spectrum rises, reaches a maximum, and decreases again towards edge-on lines of sight. The shape of the P-spectrum does not change significantly between different type-2 inclinations.

There are differences between our results of modeling a large torus (case 3 in Fig. 4) with half-opening angle $\theta_0 = 30°$, and the analogous compact torus (case 2 in Fig. 4) with identical half-opening angle but smaller dimensions. A striking difference occurs in the angular flux distribution: the large torus scatters considerably fewer photons towards an observer at intermediate viewing angles because they hit the outer parts of it (see the illustration in Fig. 7). Towards edge-on viewing directions the probability of seeing scattered photons is much lower than for the small torus. The spectral slope of the scattered radiation also differs between the two tori. While the spectrum is flat in the case of a compact torus it rises towards the red for the large torus. This can be explained by the increasing tendency of forward-scattering at shorter wavelengths. Photons escaping at higher

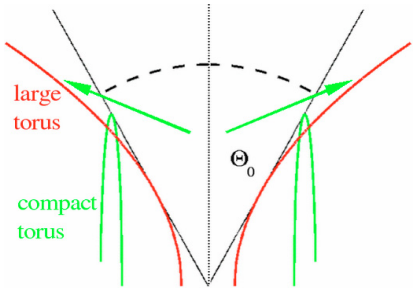

Fig. 7. Comparison of the compact and the extended torus with $\theta_0 = 30°$ in the V-band.

inclinations have to undergo back-scattering; this is more likely to happen at longer wavelengths.

There are also differences in the polarization signatures of both tori. Although the overall spectral dependence of P is the same, the level of P is changed. The strongest changes are at higher inclinations when the central source is becoming obscured by the torus. As with the total flux (see above), for the larger torus, P is significantly lower (compare the case of $i = 70°$ between the upper panels off Figs. 5 and 6). For a large torus, our current models sampling several 10^9 photons do not constrain the polarization well at very high inclinations. The number of photons scattered into these directions is too small to allow for sufficient statistics. On the other hand, it clearly follows from our computations that the spectral flux at angles $i > 76°$ is reduced by a factor of almost $\sim 2 \times 10^7$ with respect to the flux of the source. Therefore, the polarized flux at these angles is very low.

We show the differences in V-band total flux and polarization between a large and a small torus in Fig. 8. The top panel shows the polarization as a function of the viewing angle, and the bottom panel the fraction of the light reaching the observer. As was shown above, the differences between the two torus shapes are most important at higher inclinations. At $i \sim 70°$ the degree of polarization reaches a difference of 6%, and the flux differs by a factor of almost 100.

4.3. The effect of the torus half-opening angle

Kartje (1995) has shown that the half-opening angle, θ_0, of the torus is an important parameter for the obscuration and reflection properties. While modeling large tori, we examine half-opening angles ranging from 10° to 75°. Variation of θ_0 is realized by changing the vertical half-axis of the elliptical torus cross section. The other model parameters are defined as for the previous case of $\theta_0 = 30°$ in Sect. 4.2.

4.3.1. Tori with narrow or wide openings

For large tori, θ_0 is a dominant parameter for both the degree of polarization and the position angle, γ. In Fig. 9 we show the polarization of the scattered radiation as a function of wavelength and for various θ_0. Due to a similar overall shape of the wavelength dependence of P, we average the polarization over type-2 viewing angles, i, with $i > \theta_0$. We thereby exclude the highest inclinations with an insufficient number of photons, where the statistics of P are too poor. For viewing angles with $i < \theta_0$ (corresponding to type-1 objects seen face-on) the polarization is negligible.

Varying the opening angle shows several important things. For $\theta_0 < 53°$ the absolute value of the polarization decreases as the opening angle increases (see Fig. 9), as was found by

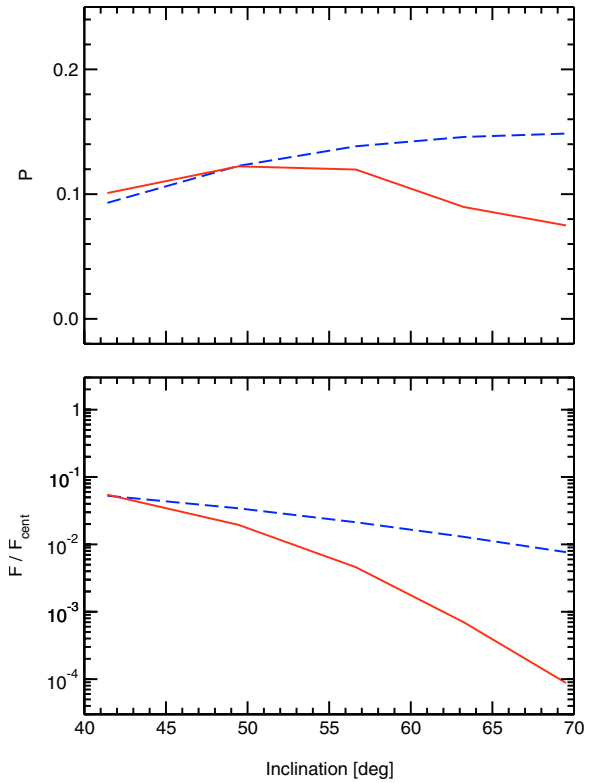

Fig. 8. Differences between large and small tori with an elliptical cross-section in the V-band (see Sect. 4.2). *Top*: polarization, P, and *bottom*, the fraction, F/F_*, of the central flux, F_*, as a function of viewing inclinations, i. The dashed lines denote the thin elliptical torus (case 2), the solid line the extended torus (case 3)

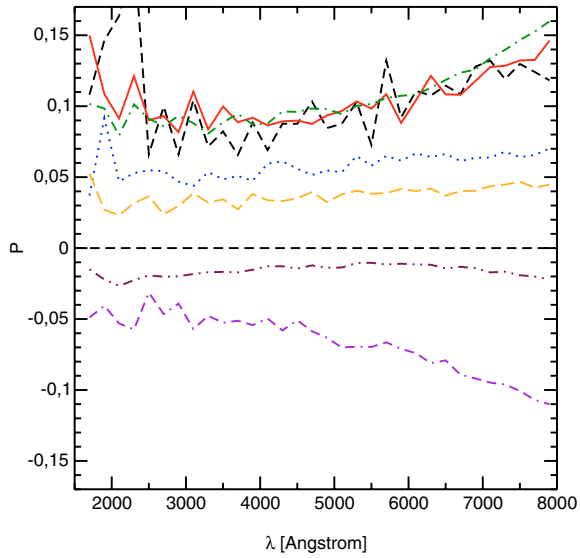

Fig. 9. Polarization averaged over type-2 viewing angles (see Sect. 4.3). A positive value of polarization denotes an $\boldsymbol{E}$-vector oriented perpendicular to the torus symmetry axis; for negative values the $\boldsymbol{E}$-vector is aligned with the projected axis. Legend: $\theta_0 = 10°$ (black dashed line), $\theta_0 = 20°$ (solid red line), $\theta_0 = 30°$ (green dot-dashed line), $\theta_0 = 45°$ (blue dots), $\theta_0 = 50°$ (long yellow dashes), $\theta_0 = 60°$ (brown double dots and dashes), and $\theta_0 = 75°$ (pink double-dashes and dots).

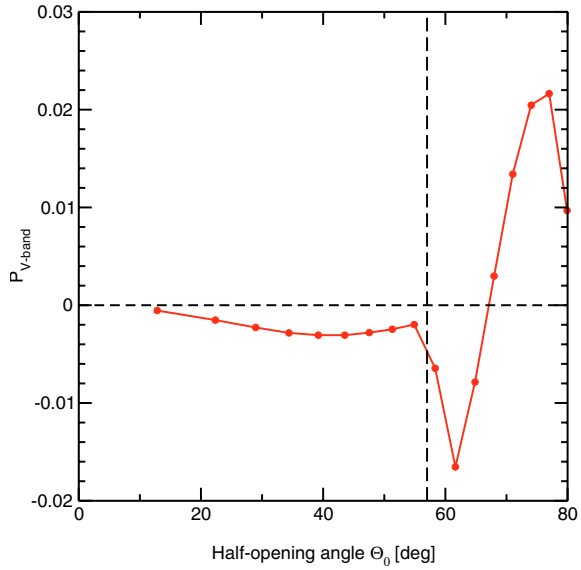

Fig. 10. Modeling an expanded torus at an intermediate opening angle of $\theta_0 = 57°$. The graph shows the polarization degree in the visual band versus inclination angle i. A positive value of polarization denotes an $\boldsymbol{E}$-vector oriented perpendicular to the torus symmetry axis; for negative values the $\boldsymbol{E}$-vector is aligned with the projected axis.

Kartje (1995) for compact tori. The polarization vector is oriented perpendicularly to the axis for all viewing directions $i > \theta_0$, as is observed in type-2 AGN. For $\theta_0 > 60°$, only parallel polarization vectors can be seen at viewing angles $i > \theta_0$. In this range of θ_0 the absolute degree of polarization increases with the opening angle.

The reason for the flip of the relative position angle can be explained by the scattering phase function, and by the geometry of the inner parts of the torus (Kartje 1995). For a distant observer looking at the torus along an off-axis line of sight, the scattered radiation comes from the inner surface walls. In part, these consist of the inner torus wall facing the observer most directly, but they also consist of the two surfaces on the side. Due to the scattering geometry, the photons scattered off the side walls are polarized along the projected symmetry axis, whilst the photons coming from the far wall are perpendicularly polarized. The ratio of the solid angle that the far side of the visible inner surface subtends to the solid angle that the visible inner side walls subtend changes with the half-opening angle of the torus, and so does the overall polarization vector.

4.3.2. Transition case: intermediate torus half-opening angles

For intermediate opening angles with $53° < \theta_0 < 60°$ the orientation of the polarization position angle seen at type-2 viewing angles depends on the exact inclination. We illustrate such a case in Fig. 10, where we set $\theta_0 = 57°$.

For a line of sight passing close enough to the horizon of the torus (i.e., when i is only moderately larger than θ_0) we find that the polarization vector is parallel, which means that type-1 polarization can be produced at obscured viewing inclinations (Fig. 10). If the inclination increases further the polarization vector switches back to type-2 polarization. It is interesting to note that such a torus can produce significant polarization degrees up to 2% for both orientations of the $\boldsymbol{E}$-vector.

In order to illustrate the integral effect of the opening angle on the polarization, we plot in Fig. 11 the polarization, $P_{\rm eff}$, averaged over all type-2 viewing positions, and over wavelength, as a function of the half-opening angle of the torus. The

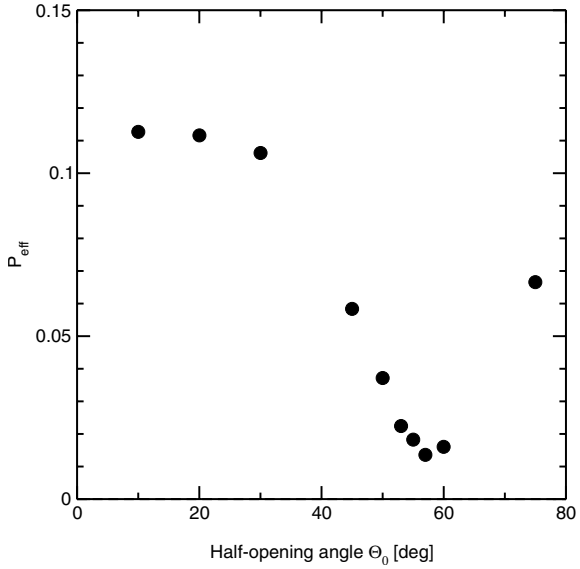

Fig. 11. Effective polarization, $P_{\rm eff}$ (see Sect. 4.3), for type-2 viewing positions as a function of the half-opening angle of an extended torus (case 3).

difference between type-1 and type-2 polarization is ignored in $P_{\rm eff}$. The absolute values of P are integrated.

The figure shows that the torus polarizes most effectively when having either a small or a large half-opening angle. In the transition region between type-1 and type-2 polarization (i.e. for $53° < \theta < 60°$) the integrated polarization goes through a minimum.

4.4. Wavelength insensitivity of polarization due to dust scattering

Wavelength-independent polarization is widely taken to be a signature of electron scattering, but we have shown in Figs. 6 and 9 that dust scattering can also produce wavelength-independent scattering. Thus a flat polarization curve is *not* a unique signature of electron scattering. As Zubko & Laor (2000) point out, the wavelength dependence of polarization provides a probe of the grain scattering properties. Inspection of the wavelength-dependent polarization curves for the large torus geometries considered above (see Figs. 6 and 9) shows that the polarization for half-opening angles with $30° < \theta_0 < 60°$ is wavelength-independent over the optical and most of the UV. For values of θ_0 outside this interval the wavelength-dependence of P is rather low and does not exceed a factor of 2. Since the scattering cross section of interstellar grains increases strongly from the optical to the UV, wavelength-independent polarization is commonly supposed to be the fingerprint of electron scattering. However, scattering in opaque dust clouds produces relatively grey scattering (Kishimoto 2001).

Our apparently contradictory result of relatively wavelength independent polarization with dust scattering arises because we are considering scattering off optically-thick material, and because of the relatively small variation of the albedo over the optical and UV spectral regions (see Fig. 3). The approximate constancy of the albedo is because the scattering and absorption cross-sections vary in a similar manner with wavelength. Since we assume an optically-thick torus, we see emergent photons that have been scattered at an optical depth $\tau \sim 1$. This is regardless of wavelength[2]. The increase in scattering cross-section with decreasing wavelength only means that the shorter wavelength photons we see have been scattered closer to the surface of the torus.

A significant change in albedo with wavelength, however, will cause a color dependency in the intensity and polarization of the scattered light[3]. Shortwards of ~2500 Å the albedo decreases, but this range is at the lower limit of the spectral range considered in our modeling. The effect can be seen in the normalized flux spectra of the torus models shown in Figs. 5 and 6. For the Galactic dust composition we implemented, it is less visible in the polarization spectra.

Another grain property that needs to be considered is the degree of asymmetry of the scattering since this is effectively an angle-dependent albedo change. Toward shorter wavelengths, Galactic dust grains are more strongly forward scattering and the polarization phase function changes (see Draine 2003). As for Thomson scattering, forward-scattered light has a lower polarization than sideways-scattered light. The polarization spectra obtained for the torus models depend on these phase functions. They additionally explain why a slight wavelength-dependence of the polarization can be found for very narrow or very wide opening angles of a large torus (see Fig. 9).

5. Polarization from polar-scattering regions

Scattering in polar regions of AGNs has allowed the discovery of hidden Seyfert-1 nuclei in type-2 objects by radiation being periscopically scattered around the obscuring torus. The central parts of the polar double cone have to be at least moderately ionized due to the intense radiation from the AGN. The medium could be associated with the warm absorber seen in many AGN (see Komossa 1999, for a review). The Doppler shift of the X-ray absorption lines indicates that the medium is outflowing at roughly 1000 $\mathrm{km\,s^{-1}}$. With increasing distance from the center, the outflow velocity and intensity of the radiation decrease. Beyond the sublimation radius, dust could also be present. However, this dust must be optically thin, as type-1 objects are not obscured.

5.1. Polar electron scattering

The polarization induced by scattering in polar, conical electron-scattering regions has been the subject of several previous studies. Brown & McLean (1977) developed a formalism to compute the polarization expected from scattering inside optically thin, axisymmetric scattering regions. This formalism was applied by Miller & Goodrich (1990) and Miller et al. (1991) to compute the polarization for polar scattering cones. Wolf & Henning (1999) and Watanabe et al. (2003) extended the modeling to optically-thick material using Monte-Carlo techniques that can account for multiple scatterings.

We confirm such results in Fig. 12 using STOKES. The figure shows the degree of polarization and the total flux as a function of the observer's inclination for an electron scattering double-cone of uniform density and with the optical depth $\tau_{\rm es} = 1$. This optical depth is measured in the vertical direction between the inner and the outer shell of one cone. In order to isolate the effects of the scattering cone from the polarization induced by the

[2] This is the reason that the sunlit sides of clouds in the earth's atmosphere are extremely white.

[3] This is the cause of colorations in the atmosphere of the giant planets.

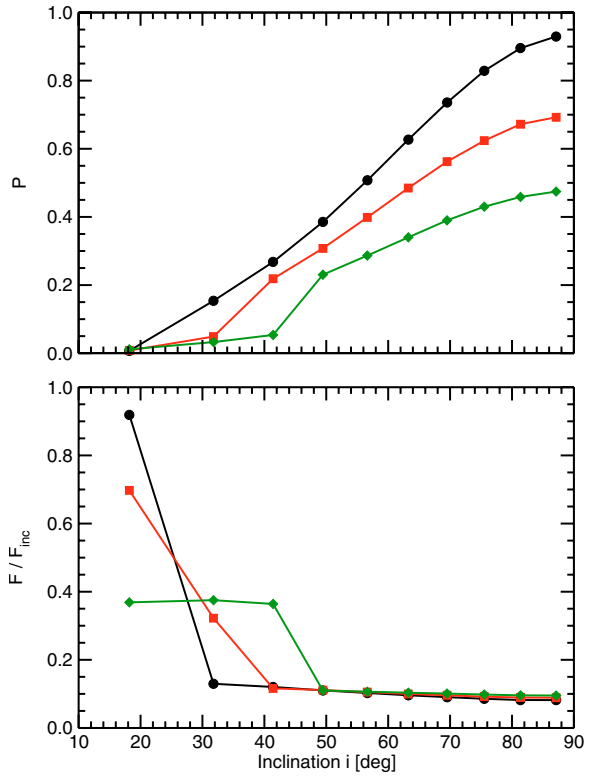

Fig. 12. Modeling double polar cones of various half-opening angles. *Top*: polarization, P, with positive values denoting type-2 polarization (perpendicular to the symmetry axis). *Bottom*: the fraction, F/F_*, of the central flux. Both values are plotted versus the inclination i with respect to the observer. The different symbols denote different half-opening angles of the double-cone. Legend: $\theta_C = 10°$ (black circles), $\theta_C = 30°$ (red squares), and $\theta_C = 45°$ (blue diamonds). The optical depth between the inner and outer shell of the cones is set to $\tau_{es} = 1$.

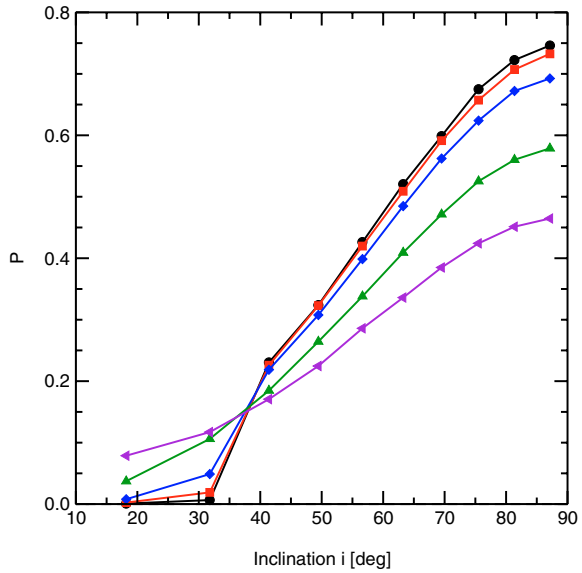

Fig. 13. Polarization degree by polar electron scattering cones with half-opening angle $\theta_C = 30°$ plotted versus the inclination i with respect to the observer. The positive values denote type-2 polarization (perpendicular to the symmetry axis). The different symbols denote different optical depths between the inner and the outer radius of the cone. Legend: $\tau_{ES} = 0.01$ (black circles), $\tau_{ES} = 0.3$ (red squares), $\tau_{ES} = 1$ (blue diamonds), $\tau_{ES} = 3$ (green triangles with points up), and $\tau_{ES} = 10$ (triangles with points left).

disk, we use an anisotropically emitting central source with the emission angles being restricted to the solid angle defined by the scattering cones. The three curves denote the half-opening angles $\theta_C = 10°$, $\theta_C = 30°$, and $\theta_C = 45°$. The inclination is measured from the symmetry axis of the double-cone.

As expected, polar electron-scattering cones produce type-2 polarization directed perpendicularly to their symmetry axis. The degree of polarization rises from face-on to edge-on viewing angles. The latter effect is due to the angle-dependent polarization phase function of Thomson scattering. For wider opening angles of the cones, the net polarization P decreases because it is the result of integrating a broader distribution of polarization vectors. The breaks of the polarization curves at $i = \theta_C$ in Fig. 12 are due to the impact of multi-scattering inside the cones, the analogous breaks in total flux curves are due to the angle-restricted central emission.

In Fig. 13 we plot the influence of the optical depth on the polarization for the polar-cones with $\theta_C = 30°$. The various curves denote different optical depths. A similar case was considered by Watanabe et al. (2003). The density of their electron cones varies with the distance from the center according to a power law. Comparison of Fig. 13 with Fig. 7 of Watanabe et al. (2003, bottom panel) shows that the difference in P is very small with respect to a uniform-density torus.

5.2. Polar dust scattering

Beyond the dust sublimation radius the scattering cone could contain dust. We investigated this using a similar bi-conical geometry and our Galactic dust prescription – see Sect. 3. In Fig. 14 we show the polarization and total flux resulting spectra for a centrally-illuminated dust cone seen at different viewing angles i. The half-opening angle of the cone has been set to $\theta_C = 30°$, and its optical depth in the V-band to the moderate value of $\tau_V = 0.3$. The strong wavelength dependence of the dust extinction properties (see Fig. 3) is clearly visible in the figure. It differs for polar viewing angles, which cross the cone, from those along equatorial directions. The former ones show the dust extinction seen in transmission, while the latter ones show dust reflection.

The total flux shown in the bottom panel of Fig. 14 is significantly reddened when $i < \theta_C$. In addition to that, the well known extinction feature at 2175 μm is seen. Its depth decreases with increasing inclination. In reflection (i.e., along equatorial viewing angles) the spectra are quite different. They peak at ~2500 Å, where the albedo goes through a maximum (see Fig. 3), and level down slowly toward longer wavelengths. This behavior is the same at all inclinations with $i > \theta_C$; the spectra differ just slightly in normalization.

The polarization spectra remain below 1% when the double-cone is seen in transmission because forward scattering does not induce significant polarization. In reflection, however, polarization becomes significant, and, for all inclinations with $i > \theta_C$, it rises towards longer wavelengths. The shapes of the spectra are, again, not very dependent on the inclination; they only differ in normalization. The highest level of polarization is obtained when the cone is seen edge-on, which corresponds to perpendicular scattering angles.

Note that, while the wavelength dependence in polarization and flux is different from the one obtained for the dusty torus

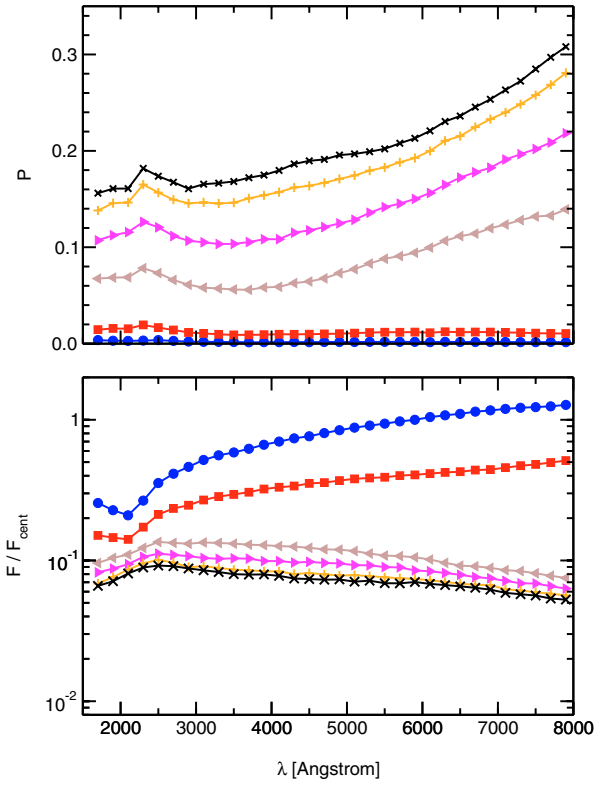

Fig. 14. Modeling a dusty double cone of half-opening angle $\theta_C = 30°$. *Top*: polarization, P. *Bottom*: the fraction, F/F_*, of the central flux, F_*, seen at different viewing inclinations, i. Legend: $i = 87°$ (edge-on, black crosses), $i = 76°$ (orange pluses), $i = 63°$ (pink triangles with points to the right), $i = 49°$ (brown triangles with points to left left), $i = 32°$ (red squares), and $i = 18°$ (face-on, blue circles).

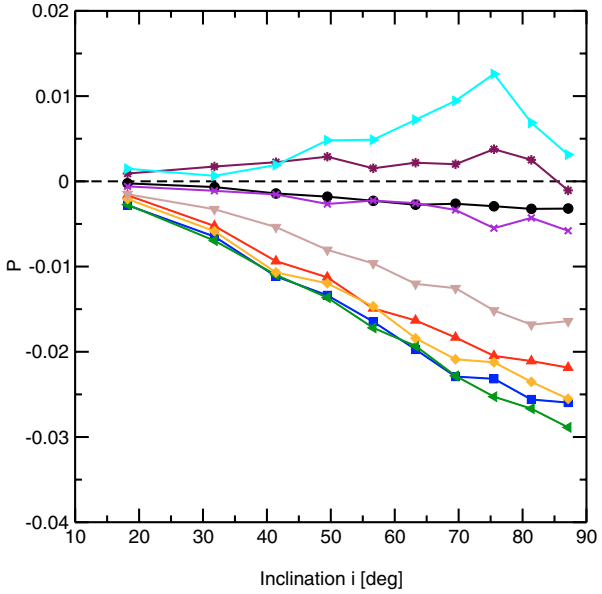

Fig. 15. Polarization versus viewing angle for a geometrically-thick emitting and scattering electron disk with $\frac{h}{d} = 0.5$. The different curves denote various vertical optical depths for the disk. Positive polarization values stand for polarization position angles perpendicular to the disk's symmetry axis, for negative values the polarization vector is aligned with this direction. Legend: $\tau_{ES} = 0.05$ (black circles), $\tau_{ES} = 0.5$ (red triangles with points up), $\tau_{ES} = 1.25$ (blue squares), $\tau_{ES} = 1$ (green triangles with points left), $\tau_{ES} = 1.5$ (orange diamonds), $\tau_{ES} = 2.5$ (brown triangles with points down), $\tau_{ES} = 5$ (purple crosses), $\tau_{ES} = 10$ (maroon stars), and $\tau_{ES} = 25$ (cyan triangles with points right).

investigated in Sect. 4 (because we are considering optically thin material in the cones), the flux rise to shorter wavelengths is still less than the rise in the cross sections.

6. Polarization from equatorial electron distributions

The major difficulty in modeling the type-1/type-2 polarization dichotomy is producing polarization *parallel* to the symmetry axis. We have illustrated above that polar scattering cones can only produce polarization vectors oriented *perpendicular* to the axis, and that the polarization produced by the dusty torus at type-1 viewing angles is mostly negligible. An exception was the case of extremely-thin tori, but these are inconsistent with the observations for at least two reasons: they are incompatible with the ratios of type-1 and type-2 objects, and very flat distributions have too low covering factors to produce the reprocessed IR emission.

It is therefore necessary to introduce a third type of scattering region. It was pointed out a long time ago that parallel polarization can be produced by a thin emitting and scattering disk (e.g., Chandrasekhar 1960; Angel 1969; Antonucci 1984; Sunyaev & Titarchuk 1985). Goodrich & Miller (1994) suggested that the parallel polarization of type-1 objects arises from scattering in a flattened equatorial medium located around the accretion disk or even the BLR. This model has been investigated in a series of papers by Young (2000), Smith et al. (2002, 2004, and 2005) using the GSM. In this model a rotating equatorial scattering disk explains the velocity-dependent polarization structure across the broad emission lines of a large sample of Seyfert galaxies very well, and also helps explaining the type-1/type-2 dichotomy. Unlike the GSM, our code includes the effects of multiple scattering, so we can consider scattering regions with higher optical depths. We first constrain possible contributions of an AGN accretion disk to the polarization (6.1). Then, we investigate with STOKES the effect of equatorial scattering disks on the continuum radiation (Sect. 6.2).

6.1. Emitting and scattering disks

We consider emitting and scattering disks with a ratio $\frac{h}{d}$ of total disk height h to diameter d. The disk is modeled in a plane-parallel approximation. It has a cylindrical shape and is uniformally filled with electrons. We consider a "thick disk" cross section with $\frac{h}{d} = 0.5$ (see Fig. 15) and a "thin disk" with $\frac{h}{d} = 0.01$ (see Fig. 16). The various curves in the diagrams refer to different vertical electron-scattering optical depths, τ_{ES}, measured vertically from the central plane to the surface. The optical depth is varied by adjusting the electron density. We investigate τ_{ES} between 0.001 and 50.

For the case of a geometrically-thick emitting disk (see Fig. 15) we find moderate polarization values of at most a few percent. The degree of polarization depends strongly on the viewing direction and the optical depth. For lower optical depth the $\boldsymbol{E}$-vector is aligned with the disk's symmetry axis. It flips to a perpendicular orientation for τ_{ES} greater ~10.

Much stronger values of the polarization can be obtained when the disk is flatter. For the geometrically-thin disk we have a similar qualitative behavior as for the thick disk (compare Fig. 16 with Fig. 15), but the degree of polarization reaches higher values and is significant even for near to face-on viewing

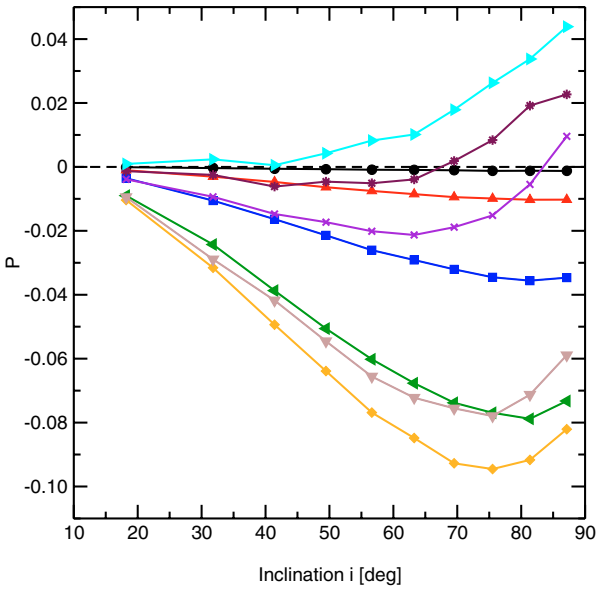

Fig. 16. Same parameters as in Fig. 15, but for a thin disk with $\frac{h}{d} = 0.01$. Legend: $\tau_{ES} = 0.001$ (black circles), $\tau_{ES} = 0.01$ (red triangles with points up), $\tau_{ES} = 0.05$ (blue squares), $\tau_{ES} = 0.2$ (green triangles with points left), $\tau_{ES} = 0.5$ (orange diamonds), $\tau_{ES} = 1$ (brown triangles with points down), $\tau_{ES} = 3$ (purple crosses), $\tau_{ES} = 5$ (maroon stars), and $\tau_{ES} = 10$ (cyan triangles with points right).

directions. The flip to perpendicular (type-2) polarization occurs at a moderate optical depth ($\tau_{ES} \sim 5$) and at an edge-on viewing angle that cannot be seen for type-1 objects. A thin disk with moderate optical depth will thus produce parallel polarization for all type-1 viewing positions.

The polarization behavior of our uniformly emitting disks can be explained in the same manner as the behavior of the polarization of the oblate spheroids examined by Angel (1969). For low τ_{ES} the net polarization is mainly determined by the photons traveling parallel to the disk plane and then being scattered towards the surface. For an observer, who does not observe the disk exactly face-on, the integrated scattered flux from the disk surface will be polarized along the projected direction of the disk axis. This can be understood by the fact that polarization by electron scattering is most efficient for orthogonal scattering angles. For the same reason, the polarization is also strongest at edge-on viewing angles.

When the optical depth becomes higher, multiple scattering of photons traveling toward the disk surface becomes relevant. The polarization vector induced by the last scattering event before leaving the disk will preferably be oriented perpendicular to the disk axis. Hence, the polarization position angle flips and on the way to this transition P becomes very low.

The emission and scattering disks investigated in this section are unlikely the cause of type-1 polarization in AGN. High enough polarization parallel to the disk symmetry axis is only produced in a disk which is geometrically *and* optically thin. While accretion disks according to the standard model of Shakura & Sunyaev (1973) are indeed geometrically thin, they are, however, optically thick. They produce too little polarization at type-1 viewing angles, as one can tell from the curves in the left part of Fig. 16. At type-2 angles the polarization can reach up to the well-known limit of ~11.7% for the highest optical depths (Chandrasekhar 1960), but with a perpendicular orientation of the polarization vector.

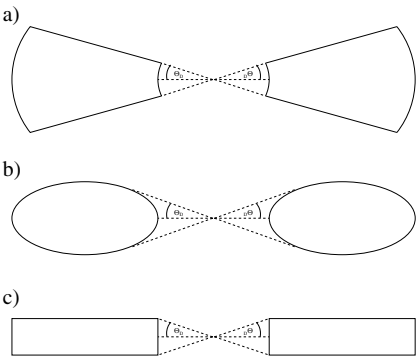

Fig. 17. The equatorial scattering geometries investigated: **a)** flared disks, **b)** tori, and **c)** equatorial cylinders. The definition of the half-opening angle θ_D is shown for each case.

6.2. Equatorial scattering wedges

Instead of scattering from the accretion disk, it has been proposed that type-1 polarization is caused by scattering by an equatorial wedge (Goodrich & Miller 1994) or by a flared equatorial disk (Smith et al. 2002). Here, we use STOKES to model such equatorial regions for different geometrical shapes and optical depths.

6.2.1. Flared disks

The geometrical shape of a flared disk of half-opening angle θ_D is given in Fig. 17a. We assume that the scattering is only off electrons. This is a good assumption for AGNs if the scattering region is located close enough to the center for hydrogen to be mostly ionized. We fix the Thomson optical depth in the equatorial plane between the inner and the outer shell, τ_{ES}, to have $\tau_{ES} = 1$.

In Fig. 18, we plot the total flux and polarization versus inclination, i, for flared disks with various half-opening angles. Both the total flux and the polarization depend significantly on the half-opening angle of the flared disk, but the polarization is always parallel to the symmetry axis of the system. The flared disk hence produces type-1 polarization, while the polarization degree obtained at type-1 viewing angles remains rather moderate at around 2%.

For viewing angles $i < 90° - \theta_D$, the central source is directly visible, which leads to higher fluxes than towards edge-on viewing angles $i > 90° - \theta_D$. If the scattering wedge crosses the line of sight, a fraction of the radiation is scattered out of the way. The polarization degree increases as the inclination goes from face-on towards edge-on viewing angles. At face-on inclinations, the line of sight is nearly aligned with the axis of the wedge and therefore the observer sees a more axisymmetric system.

For a type-1 viewing direction with $i \sim 30°$ the maximum polarization is obtained for values of θ_D in the range of 20°–30°. It turns out that changing the optical depth from $\tau \sim 1$ decreases the polarization. To illustrate this, we plot in Fig. 19 the polarization degree for a flared disk with $\theta_D = 25°$ versus the inclination i for various optical depths.

As in Fig. 18 (top), the polarization curve shows a discontinuity when the line-of-sight passes the horizon of the flared disk. However, with larger optical depths, the jump in polarization becomes shallower because multiple scattering within the disk has a depolarizing effect. For very low optical depths, $\tau < 0.1$, the scattering disk is practically invisible, as one would expect.

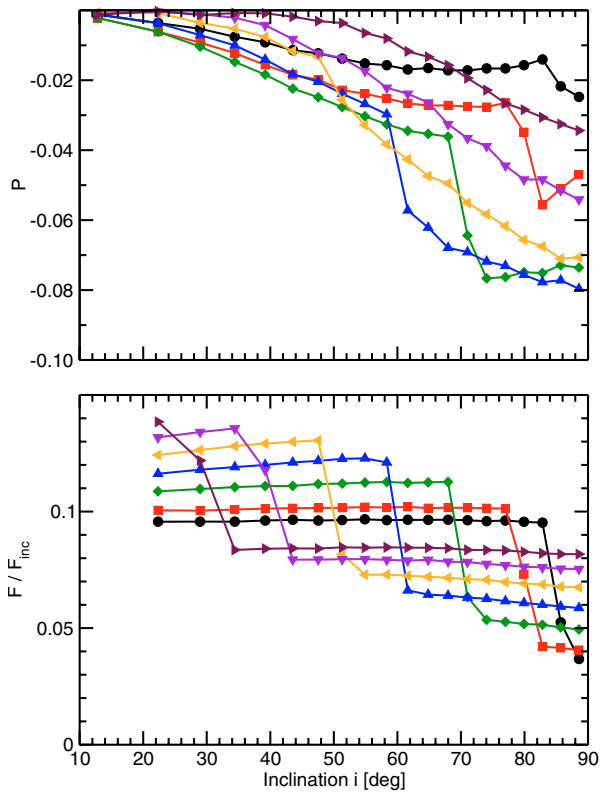

Fig. 18. Modeling equatorial flared scattering disks of various half-opening angles θ_D (see Sect. 6.2.1). *Top*: polarization, P, with negative values denoting type-1 polarization (parallel to the symmetry axis). *Bottom*: the fraction, F/F_*, of the central flux, F_*, plotted versus inclination, i, with respect to the observer. The different symbols denote different half-opening angles of the flared disk. Legend: $\theta_D = 5°$ (black circles), $\theta_D = 10°$ (red squares), $\theta_D = 20°$ (green diamonds), $\theta_D = 30°$ (blue triangles with points up), $\theta_D = 40°$ (orange triangles with points to the left), $\theta_D = 50°$ (purple triangles with points down), and $\theta_D = 60°$ (brown triangles with points to the right).

The flared disk has somewhat similar polarization properties to the emitting and scattering disks investigated in Sect. 6.1. The irradiation pattern is different but is again axisymmetric. Therefore, at low and moderate optical depths, the polarization is again mainly defined by photons traveling in a direction parallel to the disk plane being scattered at orthogonal scattering angles. As for emitting and scattering disks, this produces type-1 polarization. The central funnel of the flared disk presents a similar geometry to the dusty tori discussed in Sect. 4.3. For flat tori this produces again type-1 polarization. Because of the funnel, the source is directly visible at type-1 viewing angles, which has a strong depolarizing effect. This explains, why the net polarization of flared disks at type-1 inclinations remains rather small.

6.2.2. Other geometries

Finally, we investigate how the geometry of the equatorial scattering regions influences the polarization for the shapes in Fig. 17. For all three shapes the optical depth is defined horizontally in the equatorial plane between the inner and the outer radius of the scattering region, and fixed at $\tau_{ES} = 1$. The inner and outer radii are equal for the three different geometries, as are the half-opening angles of $\theta_D = 30°$. The inclination of the system is assumed to be at the maximal type-1 viewing angle of ~30°.

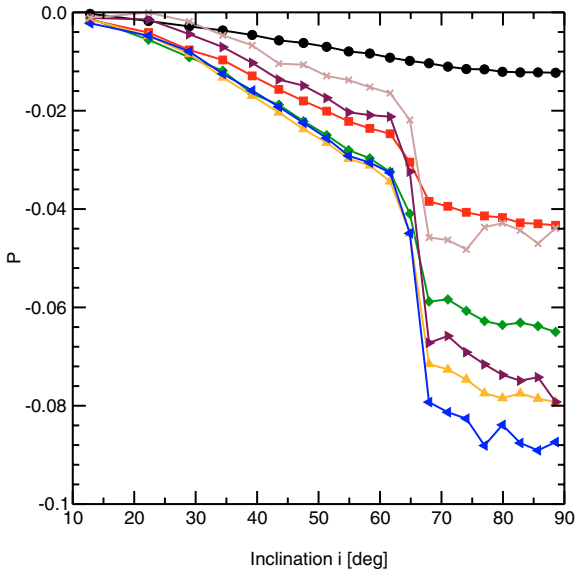

Fig. 19. The degree of polarization by electron scattering by an equatorial flared disk with half-opening angle $\theta_D = 25°$ plotted versus the inclination, i, with respect to the observer. The negative values denote type-1 polarization (parallel to the symmetry axis). The different symbols denote different optical depths between the inner and the outer radius of the disk. Legend: $\tau_{ES} = 0.1$ (black circles), $\tau_{ES} = 0.4$ (red squares), $\tau_{ES} = 0.7$ (green diamonds), $\tau_{ES} = 1.0$ (orange triangles with points up), $\tau_{ES} = 1.4$ (blue triangles with points to the left), $\tau_{ES} = 3$ (maroon triangles with points to the right), and $\tau_{ES} = 5$ (brown crosses)

.

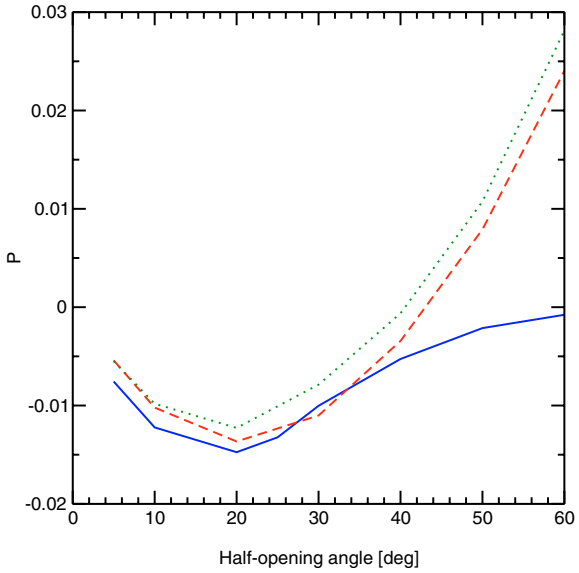

Fig. 20. The effect of the half-opening angle of the equatorial electron scattering region on polarization for three different geometries viewed from the maximal type-1 viewing position. Legend: flared disk (blue solid line), scattering cylindrical disk (dashed red line), and scattering torus (green dotted line). A negative polarization denotes polarization parallel to the axis of symmetry.

Figure 20 shows the net polarization versus θ_D, defined for the individual shapes as shown in Fig. 17. It can be seen that except for thick flared disks at large opening angles, there is a similar dependence of P on the half-opening angle. Changing the geometrical shape of the scattering disk shifts the overall level of polarization somewhat, but the dependence on the opening angle largely remains the same. In all cases the scattering regions

produce a polarization vector aligned with the axis of symmetry at type-1 viewing angles.

We have only considered the possibility of electron scattering close to the black hole, and not dust scattering, for several reasons. The main reason is that dust will not survive this close to the central continuum source. IR reverberation mapping puts the inner edge of the dusty torus just outside the broad-line region in agreement with the predicted sublimation temperature (Suganuma et al. 2006). If we replace the electrons in the models discussed in this section with dust it does not give a high enough polarization (less than around 1% even for highly-inclined viewing positions and around 0.1% at best for more likely near face-on, type-1 viewing angles) because the dust is forward scattering. Since there is absorption for dust grains the number of photons coming out is also lower than in the electron-scattering case.

In summary, the polarization arising from equatorial scattering regions has the correct orientation of the $\boldsymbol{E}$-vector for type-1 objects, but the degree of polarization remains moderate at type-1 viewing angles. This is largely independent of the geometry chosen. The low polarizations arise partly because even at maximal type-1 viewing directions the system is still close to being axisymmetric. The resulting low polarization is further decreased by dilution with the unpolarized light coming from the central source. Multiple scattering will also play a role in depolarizing the radiation. We obtained maximum polarization values for $\tau_{\rm ES} \sim 1$.

7. Discussion

7.1. Polarization from a dusty, optically-thick torus

From our modeling of uniform-density tori we obtain polarizations of a few percent from the torus alone for type-2 objects (i.e., without the need to evoke electron scattering cones – although such cones are clearly present in NGC 1068). The wavelength dependence of polarization is rather similar for different geometrical shapes of the inner torus surface. A flat surface (case 1), a slightly curved shape (case 2), or a convex shape (case 3) all reveal a nearly flat polarization spectrum over the optical and UV range for a broad range of half-opening angles. Thus, polarimetry alone does not give the geometry of dust distributions in the central regions of AGN.

We have found that the polarization is somewhat higher for a smaller steeper torus (see Fig. 8) than for a larger more gradual one. At the same time, the obscuration efficiency at type-2 viewing angles is much higher for gradually curved tori. A real torus probably has a steep inside to it. This is because the dust radius is set by dust sublimation and so will be determined primarily by the inverse square of the distance from the central source. The inside of the torus is thus probably concave towards the central source. The source creates a spherical region with a radius of the order of the sublimation radius of the dust grains, where the dust composition is likely to be very different to the dust farther away. Destruction of small dust grains will modify the grain size distribution and hence the albedo and scattering properties are likely to change. It will be an interesting future task to model polarization by scattering off a dusty torus with a more general geometry and using dust compositions different from the Galactic composition we have adopted here.

We have constrained the relation between the polarization from the torus and the opening angle (see Fig. 9). For narrow opening-angles, the polarization is stronger and has a polarization vector perpendicular to the symmetry axis. With increasing half-opening angle the polarization decreases and then gradually switches to a parallel polarization vector. Recent derivations for the number ratio of Seyfert-1 to Seyfert-2 galaxies constrain the half-opening angle of the torus to a range of $38^\circ - 48^\circ$ depending on the sample and the analysis considered (see e.g., Tovmassian 2001; Schmitt et al. 2001). Thus, for Seyfert galaxies, a realistic dusty torus can only produce type-2 polarization.

The fraction of type-2 AGNs decreases with luminosity, declining from 80% when $\log L = 42$ to 30% when $\log L = 46$. (see Ueda et al. 2003; Hasinger 2004, for recent counts). Therefore, Lawrence (1991) proposed the receding torus model, in which higher luminosities of AGNs correspond to larger torus half-opening angles θ_0. This leads to the prediction that, on average, the polarization of Seyfert-2 galaxies decreases with luminosity. The situation will be complicated by possible additional polar scattering that enhances type-2 polarization, however, there has to be a minimum amount of polarization coming from the torus alone and we predict that this decreases with luminosity. The case is different for higher luminosity quasars because there is good evidence that they have larger torus half-opening angles (see e.g. Simpson 2003). We have shown that if the torus is large and elliptically shaped, type-2 quasars with $\theta_0 > 60^\circ$ may show polarization vectors aligned with the symmetry axis. Again, this idea only holds if polar scattering is low, which does not seem to be the case for recently observed of type-2 quasars (Zakamska et al. 2005). But, in any case, the torus has to contribute to the observed polarization to some extent, and the amount of its polarization must increase with the torus opening angle. A thin, disk-like torus was considered for the high-polarization quasar OI 287 (Rudy & Schmidt 1988).

A larger opening angle of the torus corresponds to a smaller covering factor of the central source with dust. Therefore, one measure of the opening angle is the relative IR flux since it depends on the dust covering factor. We predict that the degree of polarization, on average, should be correlated with the relative strength of the thermal IR flux. So far, Smith et al. (2003) found a correlation between the K-band luminosity and the broad band optical polarization of a sample of 2MASS QSOs. Their Fig. 4 shows that QSOs with higher K-band luminosity have also higher polarization percentages in the optical and the authors point out that this could be due to more luminous or more extended scattering regions. Polarization due to scattering by a dusty torus can explain this correlation for type-2 objects: the higher K-band flux corresponds to a larger covering factor of the source and thus to a more narrow opening angle of the torus. Such tori produce higher degrees of type-2 polarization. In the data shown by Smith et al. (2003) most of the high polarization quasars are indeed of the spectral type 1.5 or 1.8−2. However, there are also a few type-1 objects that have a high K-band flux. A larger statistical sample of AGN needs to be examined for correlations between the optical polarization and the IR flux in order to draw a solid conclusion on this issue.

The lack of wavelength-dependent polarization we find is important for interpreting spectropolarimetry of type-2 AGNs. Wavelength-independent polarization is observed in the nuclei of the Seyfert-2 galaxy NGC 1068 (Antonucci & Miller 1985), for example. The wavelength independence of the polarization close to the nucleus of NGC 1068 suggests electron scattering in a polar mirror (Miller et al. 1991; Kinney et al. 1991) and even enabled a 3D-decomposition of the mirror in single electron blobs (Kishimoto 1999). However, it is difficult to maintain the ionization of the outflow, which requires an intrinsically anisotropic ionizing continuum (Miller et al. 1991). We suggest that wavelength-independent polarization also partly arises from

the walls of the torus and combines with the polar scattering. The fact that dust scattering can mimic wavelength-independent polarization has been discussed for distant radio galaxies (Dey et al. 1996; Cimatti et al. 1996), while it was stressed that a sharp drop of the dust albedo below 2500 Å should lead to a break in the polarization spectrum. In our modeling, such a feature is barely visible with the Galactic dust composition we used. However, the grain model we applied is rather simple in that it only assumes spherical grains. Most dust models of this type predict a sharp drop of the albedo below 2500 Å while observationally constrained dust albedos rise toward shorter wavelengths in the Far-UV (Gordon 2004). The ambiguity between electron scattering and dust scattering for the wavelength-dependence of polarization can hence persist even below 2500 Å.

7.2. Polarization from polar scattering cones

We have modeled polar scattering regions considering of both dust and electrons. As expected, only type-2 polarization is obtained, and the polarization degree rises towards edge-on viewing angles. Larger opening angles of the cone lead to lower polarization values. However, the results obtained here should still be used with care for the interpretation of real data. It is an implicit assumption of our modeling (and of previous modeling) that the medium is homogeneous and extends over the whole volume of the cone. This does not need to be the case as was shown for NGC 1068 in which the ionization cones are only party filled with scattering material (Capetti 1995a). For cones with larger opening angles, the detailed distribution of the material and the fact that it might be clumpy plays a role in determining the net polarization and simulations should be more detailed (Kishimoto 1996). For instance, Miller et al (1991) observe strongly wavelength-dependent polarization from a cloud near the nucleus. The polarization rises toward shorter wavelengths. This is frequently explained by dust scattering because the dust scattering cross section increases toward the blue as well. However, our computations for scattering off optically-thin dust shown in Fig. 14 reveal a different behavior. At wavelengths longer than ∼2500 Å the polarization degree seen at type-2 viewing angles decreases toward the blue because of the wavelength dependent polarization phase function (Zubko & Laor 2000). The reason that the individual cloud in NGC 1068 shows rising polarization to shorter wavelengths must therefore rely on dilution by an unpolarized blue starlight spectrum from the host galaxy.

Another important reason why the polar scattering regions should not be homogeneous is the resulting net polarization at type-2 viewing angles. If the cones have a low optical depth, the expected polarization would be very high as we show in Fig. 13. This picture can be accurate only for localized scattering regions such as the individual clouds resolved in NGC 1068 which have a polarization up to 60% (see Fig. 4 in Capetti 1995a). For distant objects, where the polar regions cannot be resolved, the observed net polarization is lower. Therefore, as Kishimoto (1996) pointed out, multiple-scattering in a clumpy medium should reduce the net polarization.

We have found in our models that the radial dependence of the scattering material inside the cones is not very important in determining the net polarization. The important parameter is the optical depth. This is true if one considers isolated cones with no other scattering mirrors involved. If one also assumes that there is an obscuring and reflecting torus, the situation must change. The torus will have a collimating effect, particularly on the central parts of the cones, so their central density becomes more important for the net polarization.

Our study of dust scattering in polar cones again underlines the importance of the optical depth for the wavelength dependence of the resulting spectra in polarization and total flux. While an optically-thick obscuring torus produces polarization that is roughly constant over the optical and UV range, scattering in cones induces a characteristic wavelength dependence. This dependence should vary with the dust composition, and future observations and modeling could constrain the dust composition.

7.3. Relative importance of toroidal and polar scattering regions

To a first approximation, the net polarization, $P_{\rm net}$, due to scattering in polar cones and scattering off the torus is given by the sum of the polarized fluxes $P_{\rm cones} \times F_{\rm cones}$ and $P_{\rm torus} \times F_{\rm torus}$ coming from the two scattering regions. This summation neglects radiative coupling between the two scattering regions, but if we take the polar cone to be optically thin, it should give a good estimate. By comparing the two single polarized fluxes, we can constrain the optical depth of the polar scattering region at which the torus becomes important for the polarization. We assume a Seyfert-2 galaxy with a torus half-opening angle of $\theta_0 = 30°$ seen at the inclination $i = 63°$. The polarized flux for the given parameters of a large torus can be derived as shown in Sect. 4. We have used the same computational method as in Sect. 5 for the polar cones. The equatorial obscuration is realized by limiting the emission angle to θ_0. We find that a polar double-cone with the same opening angle, $\theta_0 = 30°$, as the torus can have an optical depth as low as $\tau_{\rm ES} \sim 5 \times 10^{-7}$ to produce a comparable polarized flux along $i = 63°$.

We also give an estimate for the optical depth of the scattering cone needed in a Seyfert-2 system with half-opening angle $\theta_0 = 60°$ seen at an inclination of $i = 70°$. Again modeling the polarized fluxes of both components separately, we need an optical depth of $\tau_{\rm ES} \sim 5 \times 10^{-5}$ for the scattering cone to produce a comparable polarization to the torus.

Our modeling thus shows that it is not possible to independently distinguish between polarization by the torus and by polar scattering. As soon as there is even very optically thin polar scattering material, it dominates the net flux *and* polarization. The very efficient obscuration of large tori stresses the importance of polar scattering regions for the detectability of type-2 objects, and at the same time it lowers the importance of the exact polarization signature at very high inclinations. The polarized flux scattered by a torus at extreme edge-on viewing angles is so low that it hardly contributes the net polarization at all.

Both types of scattering regions are closely related, however, because the torus collimates the light entering the polar cones. Since the albedo of Galactic dust ranges between 40% and 60% a significant fraction of the light scattered in polar cones has already been scattered by the torus. To obtain the correct net polarization it is in principle necessary to conduct multi-scattering simulations involving both scattering regions. This is especially important when the base of the cone reaches far inside the funnel of the torus and has sufficient optical depth, and it remains true, even if the material in the cones is not homogeneous but organized in localized blobs as seen in NGC 1068 (Kishimoto 1999). Furthermore, the above estimate does not include any polarization induced by other scattering regions such as the accretion disk or equatorial material.

In summary, the polarization of both type-1 and type-2 AGNs arises in a complex way that will depend on the

viewing angle. We predict that the polarization properties will depend on orientation indicators such as the radio properties, the width of Hβ, and the presence of various types of intrinsic absorption-line systems.

7.4. Polarization from the accretion disk and from equatorial scattering regions

For type-1 objects, scattering from dust or electrons in the polar regions of the object only has a small impact on the observed polarization because the scattering angle is relatively small and both the covering factor and optical depth are low. Our modeling shows that polarization induced by a dusty torus is also very low along type-1 viewing angles. An additional problem is that scattering cones only produce "type-2 polarization" (i.e., perpendicular to the symmetry axis), whilst we find that tori can only give the correct polarization in type-1 quasars for large opening angles. To understand the polarization properties of Seyfert-1 galaxies, it is hence necessary to introduce additional structures to the common AGN scheme.

We have reproduced the earlier result that an emission and scattering disk can produce type-1 polarization only when it is relatively optically thin regardless its geometrical thickness. The accretion disk itself is therefore ruled out as the source of the type-1 polarization. However, the disk does give intrinsic perpendicular polarization that will be coupled successively with scattering regions such as the torus or scattering cones.

We confirm that the correct type-1 polarization can be produced by scattering of an equatorial disk, which has recently been extensively analyzed by Smith et al. (2002, 2004). The rotating BLR-disk they introduce together with the surrounding co-planar scattering region reproduces very well the turnover of the polarization vector observed in the Hα and Hβ lines of many objects (Smith et al. 2005). This gives strong support for the existence of a flattened equatorial scattering region. Recently, additional support for the idea comes from the discovery of a short timescale lag of the variations of the polarization relative to the unpolarized continuum (Shoji et al. 2005; Gaskell et al., in preparation). We find that the optical depth of the equatorial scattering material that is required to reproduce the observed polarization degree in type-1 objects is around unity, which justifies the approach of Smith et al. (2005).

An encouraging result we obtain is that the polarization properties at type-1 viewing angles do not depend very strongly on the geometry of the equatorial scattering region. This increases the flexibility in applying the flared disk model. However, according to Fig. 19 the optical depth plays a significant role in determining the polarization. Again, it will be important to consider the polarization of a flared disk in relation to the other scattering regions and model all constituents of the AGN consistently.

8. Conclusions

We have developed a versatile Monte Carlo code for modeling polarization produced by scattering in many astrophysical situations. We have shown that it reproduces previous results well. The code is publicly available and can be downloaded from the Internet.

Modeling polarization with a uniform-density torus for different half-opening angles θ_0 leads to polarization degrees between 0% and 20%. The orientation of the $\boldsymbol{E}$-vector is perpendicular to the symmetry axis for $\theta_0 < 53°$ and aligned for $\theta_0 > 60°$ at all viewing angles with $i > \theta_0$. For opening angles in the interval $53° < \theta_0 < 60°$, both orientations of the polarization vector appear at type-2 viewing angles. The polarization behavior is not strongly sensitive to details of the torus geometry (e.g. cylinders with sharp edges, versus tori with smooth elliptical cross-sections). The obscuration efficiency is much higher for a large than for a compact torus.

While the polarized flux of a torus scattered into edge-on viewing angles is rather low, we expect its polarization properties to be relevant for the collimated light entering scattering cones. This is especially important, if the scattering cones have moderate optical depths at the base. Since the opening angle of the torus and the cones increase with luminosity, we predict that the net polarization of type-2 objects depends on luminosity.

The spectral shape of the polarization produced by scattering off of a torus is nearly wavelength-independent. If a significant part of the the nuclear scattering in NGC 1068 is produced by dust in the torus then this removes the difficulty of having to maintain the degree of ionization of the putative electron cones.

Polar scattering cones produce perpendicular polarization at all viewing angles. If they contain dust the wavelength-dependence of the detected radiation is different for face-on and edge-on viewing angles. If the dusty cones are seen face-on in transmission, the spectrum is reddened and the polarization is rather low, while the scattered spectrum at edge-on directions is blue and more highly polarized.

The parallel polarization seen in type-1 AGNs arises naturally from electron scattering by optically-thin, equatorial distributions around the central source. At a given viewing angle, the polarization of different types of electron scattering disks does not depend strongly on the geometry, but it is a strong function of optical depth. A relatively low optical depth of only a few tenths can produce the observed polarization. On the other hand, optically thick equatorial material such as an accretion disk only produces type-2 polarization at all viewing angles.

All scattering regions interact, and the overall polarization properties depend on consistently modeling all components at the same time. Although the polarized flux by scattering off an optically-thick torus is weak at type-2 viewing angles, it has an important impact on the observed polarization as it collimates the radiation entering other scattering regions. The same is true for the accretion disk. The polarization properties of the individual scattering regions all strongly depend on the inclination of the system. We therefore expect, that the polarization of AGN changes systematically with orientation parameters. To quantify this prediction one needs polarization modeling for multi-component systems. Such modeling will be discussed in a follow-up article (Goosmann & Gaskell, in preparation).

Acknowledgements. We are grateful to the University of Nebraska Computer Science department for providing access to the University of Nebraska's *Prairiefire* supercomputer. David Swanson and Mako Furukawa provided valuable assistance in transferring the code to *Prairiefire*.

We wish to thank Ski Antonucci, Makoto Kishimoto, and the referee Karl Misselt, for very detailed and constructive comments on the manuscript. We also wish to acknowledge helpful discussions with Mark Bottorff and Shoji Masatoshi on the structure of AGNs, and with Tim Gay and Paul Finkler on the atomic physics of various scattering phenomena. R.W.G. thanks the Department of Physics and Astronomy of the University of Nebraska for their hospitality.

This research has been supported by the Center for Theoretical Astrophysics in Prague, by the Hans-Böckler-Stiftung in Germany, and by the US National Science Foundation through grant AST 03-07912.

References

Agol, E., & Blaes, O. 1996, MNRAS, 282, 965
Angel, J. R. P. 1969, ApJ, 158, 219
Angel, J. R. P., Stockman, H. S., Woolf, N. J., Beaver, E. A., & Martin, P. G. 1976, ApJ, 206, L5
Antonucci, R. R. J. 1982, Nature, 299, 605
Antonucci, R. R. J. 1983, Nature, 303, 158
Antonucci, R. R. J. 1984, ApJ, 278, 499
Antonucci, R. R. J. 1993, ARA&A, 31, 473
Antonucci, R. R. J. 2002, in Astrophysical spectropolarimetry, ed. J. Trujillo-Bueno, F. Moreno-Insertis, & F. Sánchez (Cambridge, UK: Cambridge University Press), 151
Antonucci, R. R. J., & Miller, J. S. 1985, ApJ, 297, 621
Blaes, O., & Agol, E. 1996, ApJ, 469, L41
Bohren, C. F., & Huffman, D. R. 1983, in Absorption and Scattering of Light by Small Particles (New York: Wiley)
Brown, J. C., & McLean, I. S. 1977, A&A, 57, 141
Capetti, A., Axon, D. J., Macchetto, F., Sparks, W. B., & Boksenberg, A. 1995a, ApJ, 446, 155
Capetti, A., Macchetto, F., Axon, D. J., Sparks, W. B., & Boksenberg, A. 1995b, ApJ, 452, L87
Cashwell, E. D., & Everett, C. J. 1959, in Monte Carlo Methods for Random-Walk Problems (Pergamon Press)
Chandrasekhar, S. 1960, Radiative Transfer (New York: Dover)
Cimatti, A., Dey, A., van Breugel, W., Antonucci, R., & Spinrad, H. 1996, ApJ, 465, 145
Cohen, M. H., Ogle, P. M., Tran, H. D., et al. 1995, ApJ, 448, L77
Czerny, B., Li, J., Loska, Z., & Szczerba, R. 2004, MNRAS, 348, L54
Dey, A., Cimatti, A., van Breugel, W., Antonucci, R., & Spinrad, H. 1996, ApJ, 465, 157
De Zotti, G., & Gaskell C. M. 1985, A&A, 147, 1
Dibai, E. A., & Shakhovskoy, N. M. 1966, Astronomicheskij Tsirkulyar, 375, 1
Draine, B. T. 2003, ApJ, 598, 1017
Draine, B. T., & Lee, H. M. 1984, ApJ, 285, 89
Ferrarese, L., Ford, H. C., & Jaffe, W. 1996, ApJ, 470, 444
Fischer, O., Henning, Th., & Yorke, H. W. 1994, A&A, 284, 187
Ford, H. C., Caganoff, S., Kriss, G. A., Tsvetanov, Z., & Evans, I. N. 1992, BAAS, 24, 818
Gaskell, C. M., & Benker, A. J. 2006, submitted
Gaskell, C. M., Goosmann, R. W., Antonucci, R. R. J., & Whysong, D. 2004, ApJ, 616, 147
Glass, I. S. 2004, MNRAS, 350, 1049
Goodrich, R. W., & Miller, J. S. 1994, ApJ, 434, 82
Goodrich, R. W., & Miller, J. S. 1995, ApJ, 448, L73
Gordon, K. D. 2004, Astrophysics of Dust, ASP Conf. Ser., 309, 77
Hasinger, G. 2004, Nucl. Phys. B Proc. Suppl., 132, 86
Heisler, C. A., Lumsden, S. L., & Bailey, J. A. 1997, Nature, 385, 700
Hines, D. C., & Wills, B. J. 1993, ApJ, 415, 82
Hines, D. C., & Wills, B. J. 1995, ApJ, 448, L69
Kartje, J. F. 1995, ApJ, 452, 565
Kay, L. E. 1994, ApJ, 430, 196
Keel, W. C. 1980, AJ, 85, 198
Kinney, A. L., Antonucci, R. R. J., Ward, M. J., Wilson, A. S., & Whittle, M. 1991, ApJ, 377, 100
Kishimoto, M. 1996, ApJ, 468, 606
Kishimoto, M. 1999, ApJ, 518, 676
Kishimoto, M., Antonucci, R., Cimatti, A., et al. 2001, ApJ, 547, 667
Komossa, S. 1999, ISAS Report, ed. T. Takahashi, & H. Inoue, 149
Lawrence, A. 1991, MNRAS, 252, 586
Lawrence, A., & Elvis, M. 1982, ApJ, 256, 410
Martel, A. 1998, ApJ, 508, 657
Mathis, J. S., Rumpl, W., & Nordsieck, K. H. 1977, ApJ, 217, 425
Mezger, P. G., Mathis, J. S., & Panagia, N. 1982, A&A, 105, 372
Miller, J. S., & Goodrich, R. W. 1990, ApJ, 355, 456
Miller, J. S., Goodrich, R. W, & Mathews, W. G. 1991, ApJ, 378, 47
Ogle, P. M., Cohen, M. H., Miller, J. S., et al. 1999, ApJS, 125, 1
Packham, C., Young, S., Hough, J. H., Axon, D. J., & Bailey, J. A. 1997, MNRAS, 288, 375
Pier, E. A., & Krolik, J. H. 1992, ApJ, 401, 99
Rowan-Robinson, M. 1977, ApJ, 213, 635
Rudy, R. J., & Schmidt, G. D. 1988, ApJ, 331, 325
Schmitt, H. R., Antonucci, R. R. J., Ulvestad, J. S., et al. 2001, ApJ, 555, 663
Shakura, N. I., & Sunyaev, R. A. 1973, A&A, 24, 337
Shoji, M., Gaskell, C. M., & Goosmann, R. W. 2005, BAAS, 37, 1420
Simpson, C. 2005, MNRAS, 360, 565
Smith, J. E., Young, S., Robinson, A., et al. 2002, MNRAS, 335, 773
Smith, J. E., Robinson, A., Alexander, D. M., et al. 2004, MNRAS, 350, 140
Smith, J. E., Robinson, A., Young, S., et al. 2005, MNRAS, 359, 846
Smith, P. S., Schmidt, G. D., Hines, D. C., & Foltz, C. B. 2003, ApJ, 593, 676
Stockman, H. S., Angel, J. R. P., & Miley, G. K. 1979, ApJ, 227, L55
Suganuma, M., Yoshii, Y., Kobayashi, Y., et al. 2006, ApJ, 639, 46
Sunyaev, R. A., & Titarchuk, L. G. 1985, A&A, 143, 374
Tovmassian, H. M. 2001, Astron. Nachr., 322, 87
Tran, H. D. 2001, ApJ, 554, L19
Tran, H. D., Miller, J. S., & Kay, L. E. 1992, ApJ, 397, 452
Tran, H. D., Brotherton, M. S., Stanford, S. A., et al. 1999, ApJ, 516, 85
Ueda, Y., Akiyama, M., Ohta, K., & Miyaji, T. 2003, ApJ, 598, 886
Walker, M. F. 1966, ApJ, 71, 184
Wang, H.-Y., Wang, T.-G., & Wang, J.-X. 2006, ApJS [arXiv:astro-ph/0609469]
Watanabe, M., Nagata, T., Sato, S., Nakaya, H., & Hough, J. H. 2003, ApJ, 591, 714
Wolf, S. 2003, ApJ, 582, 859
Wolf, S., & Henning, T. 1999, A&A, 341, 675
Young, S. 2000, MNRAS, 312, 567
Young, S., Hough, J. H., Axon, D. J., Bailey, J. A., & Ward, M. J. 1995, MNRAS, 272, 513
Young, S., Hough, J. H., Efstathiou, A., et al. 1996a, MNRAS, 281, 1206
Young, S., Hough, J. H., Efstathiou, A., et al. 1996b, MNRAS, 279, L72
Young, S., Corbett, E. A., Giannuzzo, M. E., et al. 1999, MNRAS, 303, 227
Zubko, V. G., & Laor, A. 2000, ApJS, 128, 245
Zakamska, N. L., Schmidt, G. D., Smith, P. S., et al. 2005, AJ, 129, 1212